Results from In-Package Alloy Electrochemical Corrosion Experiments: Implications for Long-Term Spent Fuel Degradation

Spent Fuel and Waste Disposition

Prepared for
US Department of Energy
Spent Fuel and Waste Science and Technology
James Jerden
Eric Lee
Vineeth Kumar Gattu
William Ebert
Argonne National Laboratory
March 19, 2019
ANL/CFCT-19/2

This work was supported by the US Department of Energy, Office of Nuclear Energy. The report was prepared at Argonne National Laboratory as part of the Spent Fuel and Waste Science and Technology Campaign.

EXECUTIVE SUMMARY

This work is being performed as part of the DOE NE Spent Fuel and Waste Science and Technology Campaign, Argillite and Crystalline Rock R&D work packages: SF-19AN01030101 and SF-19AN01030201. This document meets the milestone M3SF-19AN010301012 for Argillite R&D and the milestone M3SF-19AN010302012 for Crystalline R&D.

The fuel matrix degradation (FMD) model calculates the degradation rate of spent UO2 fuel based on fundamental electrochemical theory and thermodynamics. The model provides the quantitative basis for radionuclide source term predictions in the generic disposal system analysis (GDSA) performance assessment (PA) model. The FMD model has been implemented in a manner that facilitates its integration with the GDSA-PA code and a preliminary, integrated FMD-GDSA model has been successfully tested (Jerden et al., 2017). The specific focus of on-going work is to accurately and quantitatively represent the generation of H_2 in a breached waste package and model its effect on the degradation rate of the spent fuel so that this key process can be accurately represented in PA models.

It has been shown experimentally that millimolar concentrations of dissolved H_2 in contact with spent fuel will inhibit oxidative dissolution and decrease the fuel degradation rates by 3 – 4 orders of magnitude (e.g., Röllin et al., 2001, Ollila, 2008). This will lead to a significant decrease in the radionuclide source term values used in repository PA models. Sensitivity studies using the FMD model have shown that the dissolved H_2 concentration is the dominant environmental variable affecting the UO_2 spent fuel dissolution rate (Jerden et al., 2015). Therefore, on-going experimental and modeling efforts focus on H_2 production, accumulation and interfacial reactions within a breached waste package.

The anoxic corrosion of metallic engineering materials will be the main source of H_2 in crystalline and argillite rock repository systems, including stainless steel, carbon steel, and aluminum internal waste package components and possibly the Zircaloy fuel cladding. A steel corrosion module was added to the FMD model to account for these H_2 sources and couple the H_2 generation rate with fuel degradation processes (Jerden et al., 2017). As discussed below, there is a need for experimental data from electrochemical corrosion experiments with relevant steel, Zircaloy and UO_2 electrodes to parameterize and validate the steel corrosion module in the FMD model with regard to the effects of key environmental variables (Eh, pH, concentrations) and alloy compositions on the H_2 generation rate.

This report presents results from a series of electrochemical corrosion tests that provide information needed to parameterize and validate the FMD model. The alloys tested include 316L stainless steel (316SS), AISI 4320 carbon steel (C-steel), Zircaloy-4 fuel cladding (unirradiated) and a borated aluminum composite material (Boral). Potentiodynamic polarization tests were performed in buffer solutions at pH 4, 7 and 10 with NaCl concentrations of 0, 4 and 100 millimolar (mM) and potentiostatic tests were completed in the 4 mM solutions.Other tests are in progress. All tests were performed at laboratory ambient temperatures (~22^{o}C). These electrochemical tests provide new insights into the corrosion behavior of these key alloys in solutions that represent possible seepage waters. The primary findings are as follows:

- The 316L and Zircaloy passivated rapidly under all conditions, but passivation broke down in high NaCl solutions within a few days under some Eh-pH conditions.
- Chloride concentrations of 100 mM (as NaCl) are sufficient to break down passivating oxide layers that form on 316L stainless steel at potentials greater than 0.5 V_{SHE} at pH 4 and at potentials greater than 0.85 V_{SHE} at pH 7 and 10.
- The measured steady state corrosion rate of 316L stainless steel ranged from 0.004 to 0.2 μm/yr in 4 mM NaCl solutions.

- Carbon steel (AISI 4320) undergoes rapid, active corrosion (100 mm/yr) in pH 4 solutions regardless of NaCl concentration.
- At pH 7 and pH10 the corrosion rate of C-steel is slowed by the presence of an oxide layer (magnetite); however, this layer breaks down above 0.3 V_{SHE} at pH 7 and 0.1 V_{SHE} at pH 10 in solutions containing 100 mM NaCl.
- The measured corrosion rates for C-steel vary from 16 mm/yr to 140 mm/yr.
- Zircaloy-4 samples show relatively low corrosion rates (0.04 – 2 μm/yr) over the full pH (4 – 10) and chloride concentration range (0 – 100 mM) due to the presence of zirconium oxide on the surface. The high corrosion rate was measured at pH 10.
- The borated aluminum composite Boral was shown to undergo rapid, active corrosion with estimated corrosion rates on the same order as C-steel (≥100 mm/yr). The actively corroding phase in Boral is aluminum metal that serves as a matrix for boron carbide particles. The B_4C particles do not appear to have corroded in any of the tests (pH 4, 7, 10), but are physically removed from the material as the surrounding Al matrix is removed by corrosion.
- Tests performed on Boral and pure aluminum (Al-1100) at pH 10 yield low corrosion rates (0.5 – 10 mm/yr) relative to results from the pH 4 and pH 7 tests at potentials below 0 V_{SHE} (based on potentiodynamic data). This is due to formation of an aluminum hydroxide layer that slows cathodic reactions at the alloy surface.

The corrosion rates measured during the electrochemical tests were used as direct input to a new FMD/in-package chemistry model that is being developed to provide accurate long-term spent fuel degradation rates as chemical conditions (Eh, pH, speciation) evolve within a breached waste package. This new model was developed for the present study by coupling the FMD model with the reactive transport code X1t, which is a module within the Geochemist's Workbench (GWB) reaction path modeling code. The reactive transport model consists of a 1D domain discretized with 21 reaction diffusion cells and includes a single waste package cell, two cells within the bentonite backfill, and 19 other cells within the near-field host rock.

The reactive transport model has been used successfully to calculate the amount of H_2 produced and accumulated within a breached waste package due to the corrosion of stainless steel, carbon steel and aluminum alloys based on the experimental result mentioned above. The GWB in-package model accounts for the masses, surface areas and corrosion rates of each alloy and tracks all relevant chemical speciation reactions to provide information on in-package pH, Eh and chemistry for a 10^5 year generic repository simulation. The model accounts for both the diffusive and advective transport of dissolved H_2 away from the waste package. The concentration of dissolved H_2 is the key variable in the FMD model, therefore, being able to accurately model the evolution of H_2 within the waste package is essential for accurately predicting long-term spent fuel degradation rates.

The dissolved concentrations of H_2 predicted by the GWB in-package model are directly input into the FMD model, which is run to determine the spent fuel degradation rates as a function of time. The initial sensitivity runs performed with this combined GWB - FMD model resulted in the following predictions:

- In cases with around 6000 kg of 316 SS per waste package (typical for U.S. waste package designs envisioned the Yucca Mountain repository) and no advection, the slow corrosion of 316SS generates enough H_2 per year to maintain H_2 concentrations higher than the threshold needed to inhibit spent fuel degradation by oxidative dissolution. This occurs even in cases where the C-steel and aluminum alloys (Al-6061) are completely consumed within 100 years of the waste package breach.
- Advective flow through the breached waste package causes the H_2 concentration in the in-package solution to decrease to values lower than the threshold needed to suppress oxidative dissolution. In these cases, with advective flow, spent fuel degradation is slow (and governed by chemical

dissolution rates) as long as there is appreciable C-steel and Al-6061 present. the fuel degradation rates will increase significantly due to radiolytically driven oxidative dissolution processes once these alloys are consumed by corrosion.

This page is intentionally left blank.

This page is intentionally left blank.

LIST OF FIGURES

LIST OF TABLES

ACRONYMS

BWR	Boiling Water Reactor
DOE	U.S. Department of Energy
FEPs	Features, events, and processes
FMD	Fuel matrix degradation (model)
FMDM	Fuel matrix degradation model
GDSA	Generic Disposal System Analyses
MCNPX	Monte Carlo N-Particle eXtended
ORNL	Oak Ridge National Laboratory
PA	Performance assessment
R&D	Research and development
SEM	Scanning electron microscopy
SCE	Saturated calomel electrode
SHE	Standard hydrogen electrode
SFWS	Spent Fuel and Waste Science and Technology (campaign)
SNF	Spent nuclear fuel
STAD	Standardized Transportation, Aging and Disposal Canister

This page is intentionally left blank.

SPENT FUEL AND WASTE SCIENCE AND TECHNOLOGY CAMPAIGN

1. INTRODUCTION AND OBJECTIVE

The purpose of this project is to develop, test and implement a process model for the degradation rate of spent nuclear fuel that can be readily incorporated into the generic disposal system analyses (GDSA) performance assessment (PA) code to provide reliable radionuclide source terms over the service life of a deep geologic repository. The fuel matrix degradation (FMD) model (or FMDM) is an electrochemical reactive-transport model based on fundamental redox kinetics and thermodynamics that was developed for this purpose and is currently being updated and tested. The FMD model isbased the Canadian Mixed Potential Model (CMPM) of Shoesmith and King, 1998, Shoesmith et al., 2003 and King and Kolar 2003, but has been expanded to account for key phenomena (e.g., H_2 interfacial reactions) and customized for application in the ongoing spent fuel and waste science and technology (SFWS) campaign.

The continuing development and implementation of the FMD model address two high level Features, Events, and Processes (FEPs) that are recognized as high R&D priorities for the SFWS campaign (Wang et al., 2014). The FEPs addressed by this model are 2.1.02 (waste form) and 2.1.03 (waste container), which correspond to the high priority research topics P19 (Development of waste form degradation model) and P20 (Development of new waste package concepts and models for evaluation of waste package performance for long-term disposal) identified by Wang et al., 2014.

Specifically, the FMD model uses mixed potential theory to calculate the degradation rate of UO_2 by accounting for all major anodic and cathodic interfacial reactions. Other major phenomena that are represented in the FMD model include:

- The effect of hydrogen generated from steel corrosion within a breached waste package,
- Alpha radiolysis and the generation of radiolytic oxidants as a function of fuel burn-up,
- Growth a porous layer of uranyl oxyhydroxide and/or uranyl peroxide corrosion phases.
- Complexation of dissolved uranium by carbonate.
- Temperature variations of reaction rates (by Arrhenius equations),
- One-dimensional diffusion of all chemical species to and from the fuel and steel surfaces.
- Bulk solution reactions such as the oxidation of ferrous iron by O_2 and radiolytic H_2O_2.

The most important process included in the FMD model that was not addressed in the original CMPM is the oxidation of dissolved hydrogen at the spent fuel surface (Jerden et al., 2015). Leaching experiments with spent fuel and simulated spent fuel have shown that the presence of H_2 generated during the corrosion of steel added to a test can decrease the fuel degradation rate by 3 - 4 orders of magnitude relative to tests performed with no steel present (e.g., Röllin et al., 2001, Ollila, 2008). The means by which the effect of H_2 is represented in the FMD model is discussed in Section 2 below.

Jerden et al., 2017 discussed the addition of a corroding steel surface as a source of H_2 to the FMD model (FMDM version 3). One of the main findings of that work is that the extensive coupling between the corrosion of waste package components and the spent fuel that must be taken into accounted to accurately predict radionuclide source terms. As discussed in Jerden et al., 2017, the Eh and pH conditions within a breached waste package will evolve with time due to coupled reactions of alloy corrosion, radiolysis, and spent fuel dissolution. The latest FMD model includes a first step towards including the coupled processes

by linking steel corrosion kinetics and fuel degradation rates; however, more extensive experimental and modeling work is needed to accurately model the dynamics of fuel degradation and in-package chemistry. The present report updates the work discussed in Jerden et al., 2017 and Jerden et al., 2018 and provides discussion of ongoing experimental work to measure parameter values and dependencies for the latest version of the FMD model (FMDM version 4). The electrochemical experiments that are being performed to parameterize the FMD model (V.4) are discussed in Section 3 below.

As summarized in Jerden et al., 2017 and Jerden et al., 2018, the FMD model has been successfully integrated with the GDSA-PA code PFLOTRAN; however, there is a need to optimize the integrated code to improve computing speed. The flow of information within the integrated FMDM – GDSA-PA model is summarized in Figure 1.

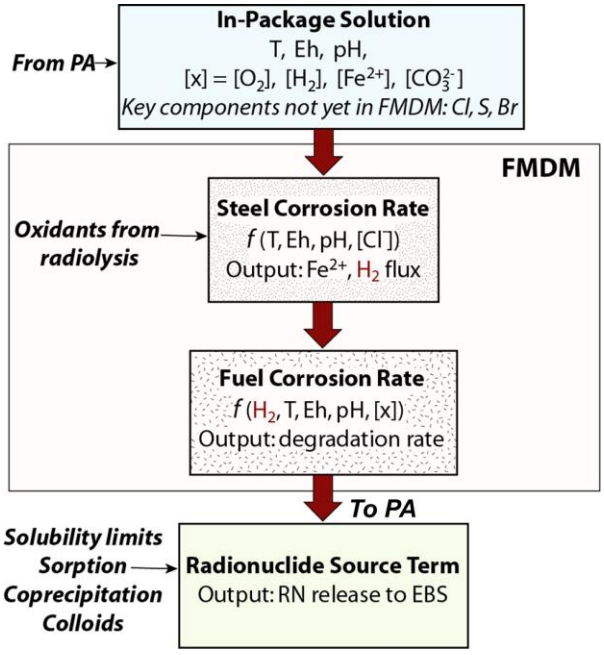

Figure 1. Schematic summary diagram showing the context of the FMD model within the source term calculation information flow (adapted from Jerden et al., 2017).

2. THE FUEL MATRIX DEGREDATION MODEL

The FMD model is based on fundamental electrochemical principals, employing Butler-Volmer relationships, mixed potential theory and traditional mass balance and reactive transport relationships (King and Kolar, 1999) to determine the degradation rate of the fuel. Specifically, the FMD model calculates the dissolution rate of spent fuel as a function of the interfacial corrosion potential (E_{corr}), at which all of the anodic and cathodic half reactions occurring at the fuel/solution boundary are kinetically balanced with no net electron transfer. The dissolution rate (which corresponds to an anodic current due to the oxidation of U^{4+} to U^{6+}) is relatively high under oxidizing conditions above the U(IV)/U(VI) threshold potential, but significantly lower at potentials where only solubility-limited chemical dissolution of U^{4+} occurs.

The threshold potential for U(IV)/U(VI) oxidative dissolution depends on pH, as shown in Figure 2, and on the water chemistry. Under the reducing conditions envisioned in argillite and crystalline rock repositories (the region in Figure 2 labeled Repository Groundwater), the Eh of the solution will be well below the U(IV)/U(VI) threshold. However, the radiolysis of water by spent fuel to form H_2O_2 and O_2 can cause localized oxidizing conditions that drive the Eh far above the threshold for oxidative dissolution of the fuel, i.e., into the U(VI) stability field. The shaded area in Figure 2 shows the possible range of in-package conditions due to radiolysis (which affects Eh) and the corrosion of steel components (which affects Eh and pH). This indicates that the FMD model must address a range of pH from about 4 to 11 and Eh values spanning the range of water stability.

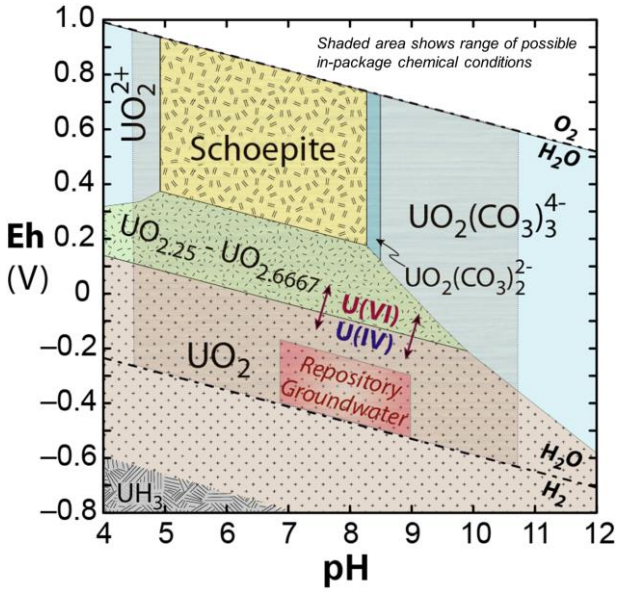

Figure 2. Pourbaix diagram for uranium speciation showing the conditions expected for groundwaters in a reducing crystalline rock or argillite repository (red region, from Laaksoharju, et al., 2008) and conditions due to radiolysis (shaded gray region). This diagram was drawn for a solution with $1x10^{-6}$ molar uranium and $1x10^{-4}$ molar carbonate. Eh is relative to standard hydrogen electrode (SHE).

A number of experimental and modeling studies have shown that the oxidative dissolution of spent fuel in anoxic environments is counteracted by the catalyzed oxidation of H_2 on fission product alloy phases referred to as Ru ε-phases or noble metal particles (NMP) (e.g., Broczkowski et al., 2005, Shoesmith, 2008, Grambow, et al., 2010). What we refer to as the H_2 effect has been shown qualitatively to decrease spent fuel dissolution rates by up to 4 orders of magnitude from the maximum rates attained in the absence of H_2.

The major goal of the ongoing FMD model development work is to implement an accurate model that quantifies the generation and accumulation of H_2 and its effect on spent fuel degradation rates.
The two main sources of H_2 in the repository will be: (1) the radiolysis of in-package solutions, and (2) the anoxic corrosion of steels and other alloys present in within the breached waste package and in the surrounding EBS and nearfield. Of these sources, alloy corrosion has been shown to be dominant (e.g., Johnson and King, 2003, Turnbull, 2009). Therefore, to accurately represent the effect of H_2 on spent fuel degradation rates we must account for alloy corrosion within a breached waste package. To this end, the FMD modeling work has expanded to include the quantification of alloy corrosion as a source of H_2 (e.g., Jerden et al., 2017, Jerden et al., 2018).

Our on-going work addresses the coupling between the corrosion of waste package components and the spent UO_2 fuel. As shown in Jerden et al., 2017, the Eh and pH conditions within a breached waste package will evolve with time due to coupled reactions of alloy corrosion, radiolysis, and spent fuel dissolution. The latest FMD model accounts for radiolysis and takes a step towards accounting for coupled processes by linking steel corrosion kinetics and fuel degradation rates; however, more experimental and modeling work is needed to more accurately model the dynamic relationship between spent fuel degradation and in-package alloy corrosion.

2.1 Fuel Degradation Model Reaction Scheme

The key processes represented in the latest version of the FMD model include:

- The generation of radiolytic oxidants as a function of fuel burn-up,
- NMP(ε-phase)-catalyzed oxidation of H_2, which protects the fuel from oxidative dissolution,
- The precipitation and growth of a uranyl oxyhydroxide (schoepite) corrosion layer that blocks radiolysis at the fuel/solution interface and slows the diffusion of reactants to and from the fuel surface,
- The complexation of uranyl by carbonate,
- The destruction of O_2 and radiolytic H_2O_2 by ferrous iron within the bulk solution,
- Temperature variations of reaction rates (by Arrhenius equations),
- The one-dimensional diffusion of all chemical species to and from the fuel and steel surfaces,
- The anoxic corrosion of steel components to generate dissolved H_2 and ferrous iron.

As discussed above, the effect of H_2 oxidation is the most important of these processes for determining the fuel dissolution rate and the radionuclide source terms (Jerden et al. 2015). The second most important effect is the oxidative dissolution of the fuel by the radiolytic oxidant H_2O_2 and its decomposition product O_2. In the FMD model, the H_2O_2 concentration is calculated using an analytical form of the radiolysis model developed at PNNL (Buck et al., 2014) and a burn-up/dose rate function derived from Radulescu, 2011.

The reaction scheme and layout of the FMD model is shown in schematically Figure 3.

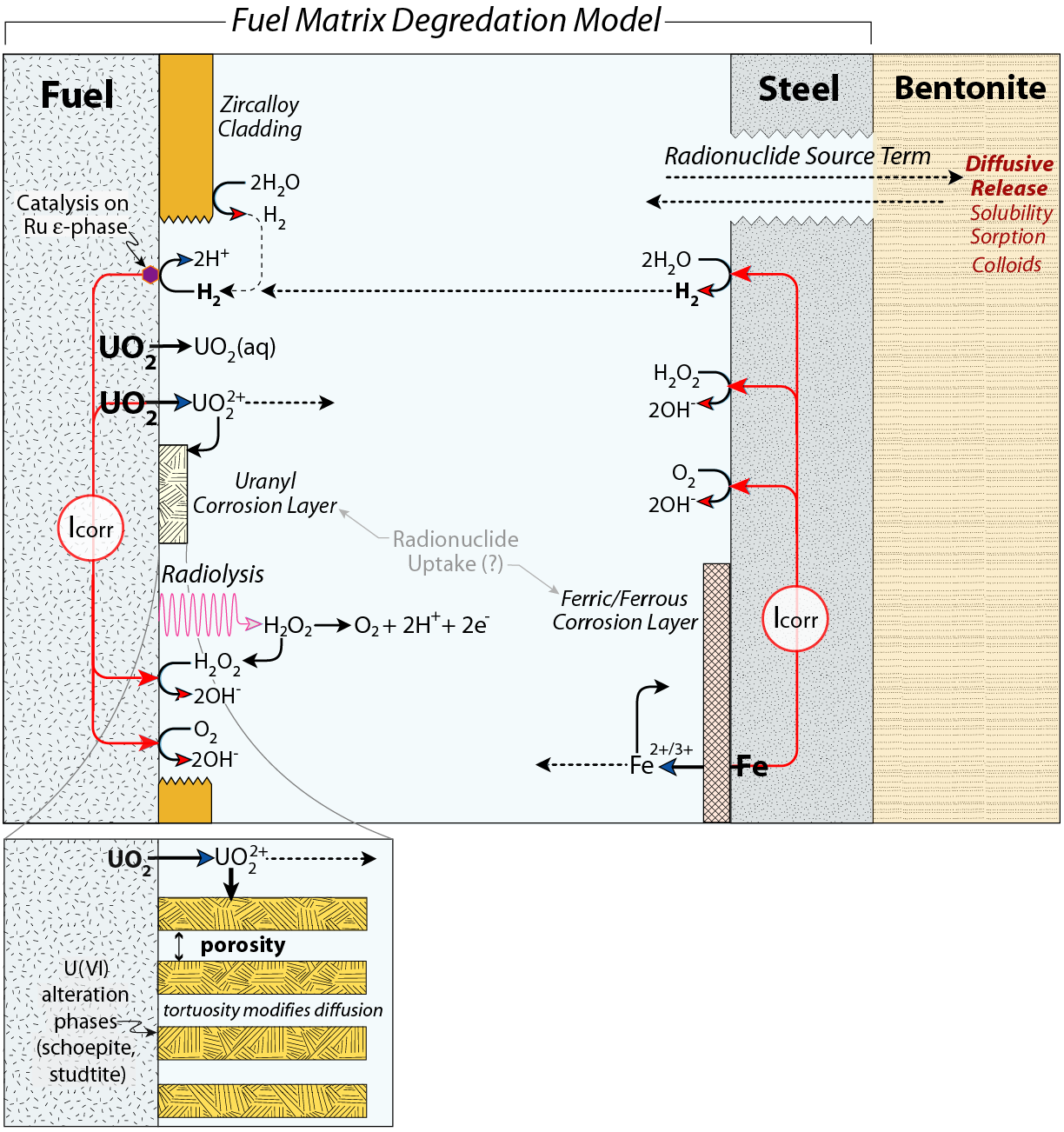

Figure 3. Schematic diagram showing the reaction scheme for the fuel matrix degradation model and identifying other key processes that influence in-package chemistry and radionuclide mobilization (I_{corr} indicates corrosion current).

The specific steps involved in radionuclide release from spent fuel that are or will be represented in the FMD model are as follows:

- In a breached waste package, groundwater will infiltrate open spaces within the canister and begin to corrode in-package alloys.
- Alloy corrosion will produce H_2 even when the infiltrating groundwaters are electrochemically reducing with respect to the fuel. This is because the stability fields of

carbon steels and stainless steels lie below the stability field of water, as shown in Figure 4.

- Assuming that the Zircaloy cladding has also been breached, the fuel will begin degrading when contacted by seepage water by either relatively rapid oxidative dissolution (~1 - 10 g/m^2 yr) or by relatively slow chemical dissolution ($\leq 10^{-3}$ g/m^2 yr), depending on the Eh and pH of the seepage water and the dissolved concentration of H_2.

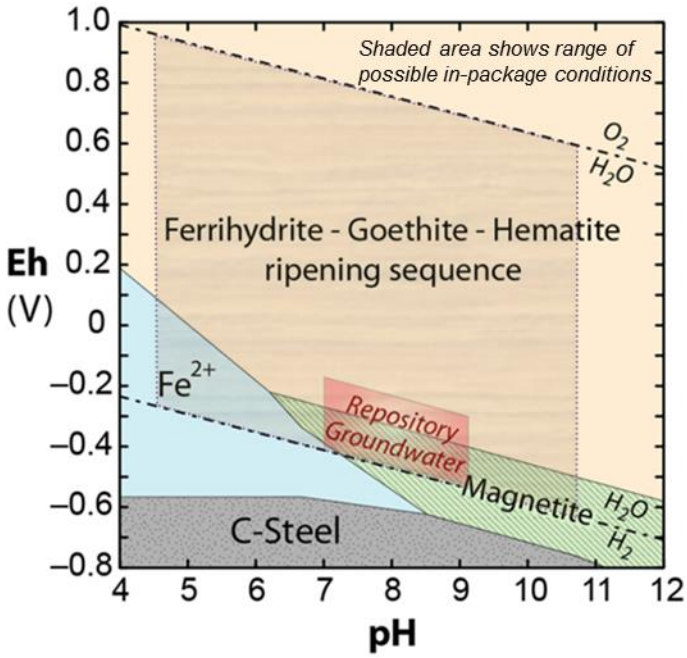

Figure 4. Pourbaix diagram showing the conditions expected for groundwaters in a reducing crystalline rock or argillite repository (red region, from Laaksoharju, et al., 2008) and conditions due to radiolysis (shaded gray region).

2.2 Breached Waste Package Environment

Figures 5 and 6 are simplified conceptual diagrams of a typical spent fuel waste package in a generic crystalline or argillite repository setting (adapted from Energy Solutions, 2015). These figures highlight the spatial context and key processes that the FMD model represents. As shown in Figures 5 and 6, the spent fuel assemblies will be surrounded by (and in close contact with) a number of alloy components within the waste package. These materials include C-steel, 316SS and either borated aluminum or borated steel alloys. Another important material from the prospective of H_2 production in the repository is the Zircaloy cladding retaining the fuel pellets (gold or yellow in Figures 5 – 6). No credit is taken for Zircaloy as a barrier to radionuclide release in the current FMD or GDSA PA models, however Zircaloy corrosion should be included in the FMD model because it could represent an important source of H_2. Quantifying the effect of Zircaloy corrosion in the FMD model is a subject of ongoing model development work.

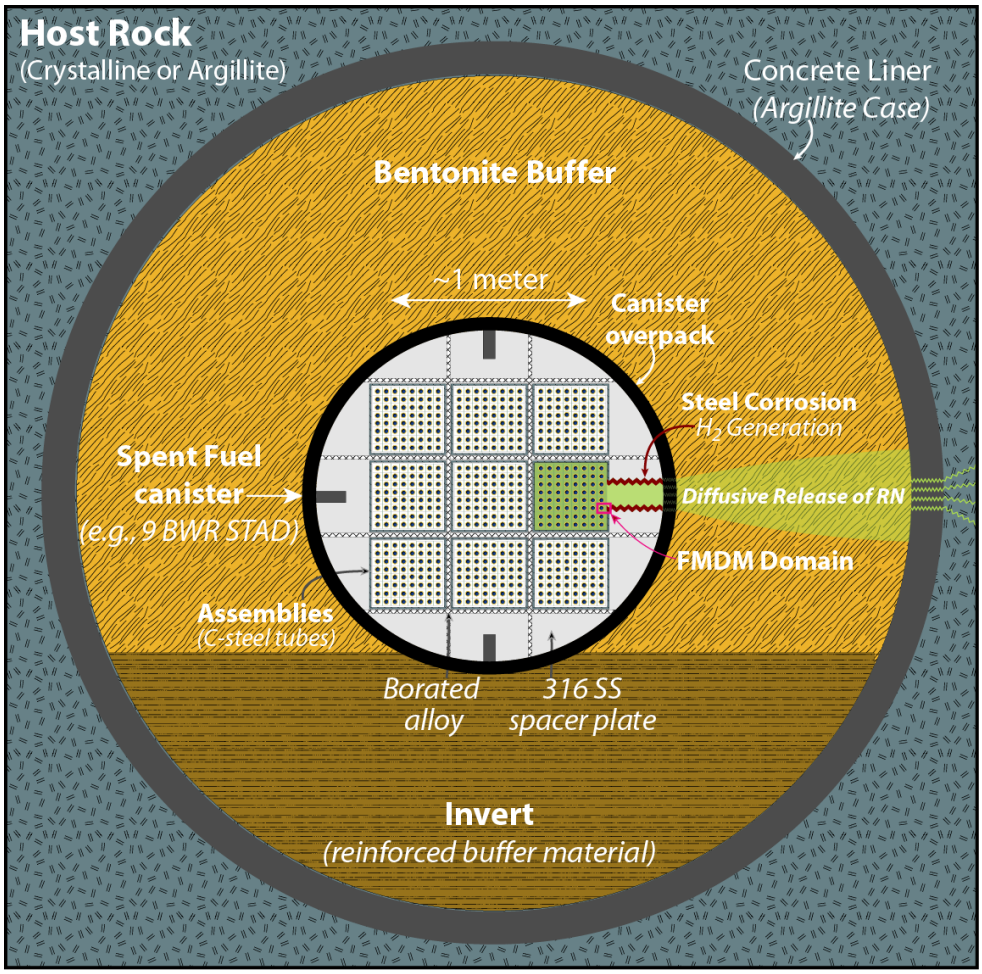

Figure 5. Conceptual diagram of a generic waste package showing a conceptual canister-breaching scenario. BWR STAD denotes a boiling water reactor standard transport, aging and disposal canister and RN denotes radionuclides (adapted from Energy Solutions, 2015).

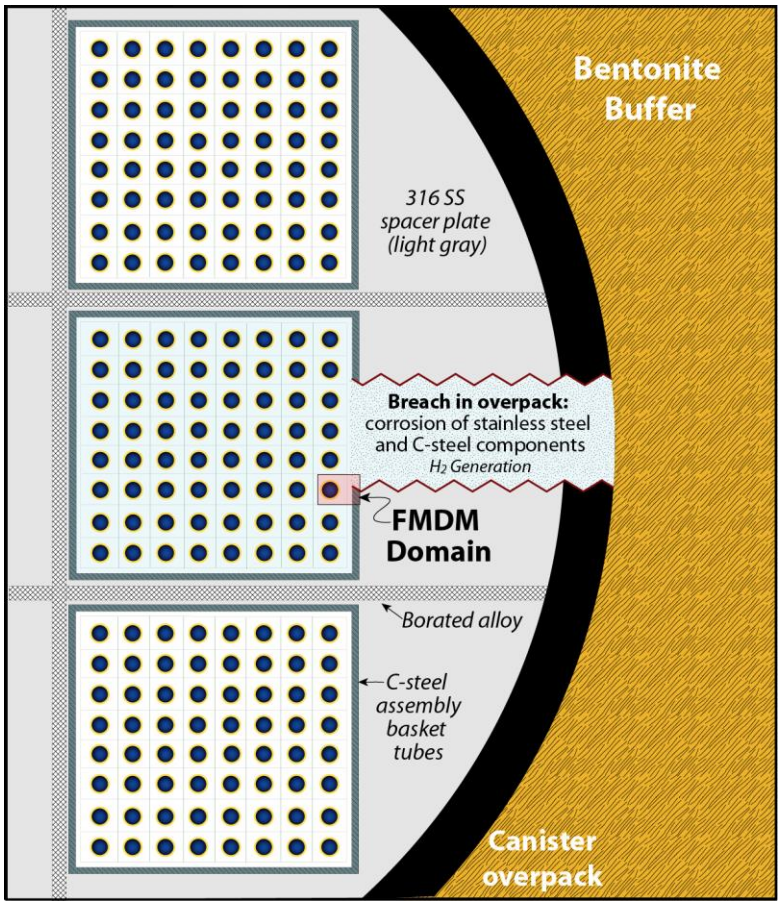

Figure 6. Conceptual diagram of a generic waste package showing a conceptual canister-breaching scenario (adapted from Energy Solutions, 2015).

A schematic diagram showing the key materials and important reactions within a breached spent fuel waste package is shown in Figure 7. This figure highlights the chemical coupling between spent fuel degradation and the corrosion of alloys within a breached waste package (in-package solution). There will also be feedback between the in-package chemistry and reactions occurring within the bentonite and other EBS and near-field materials.

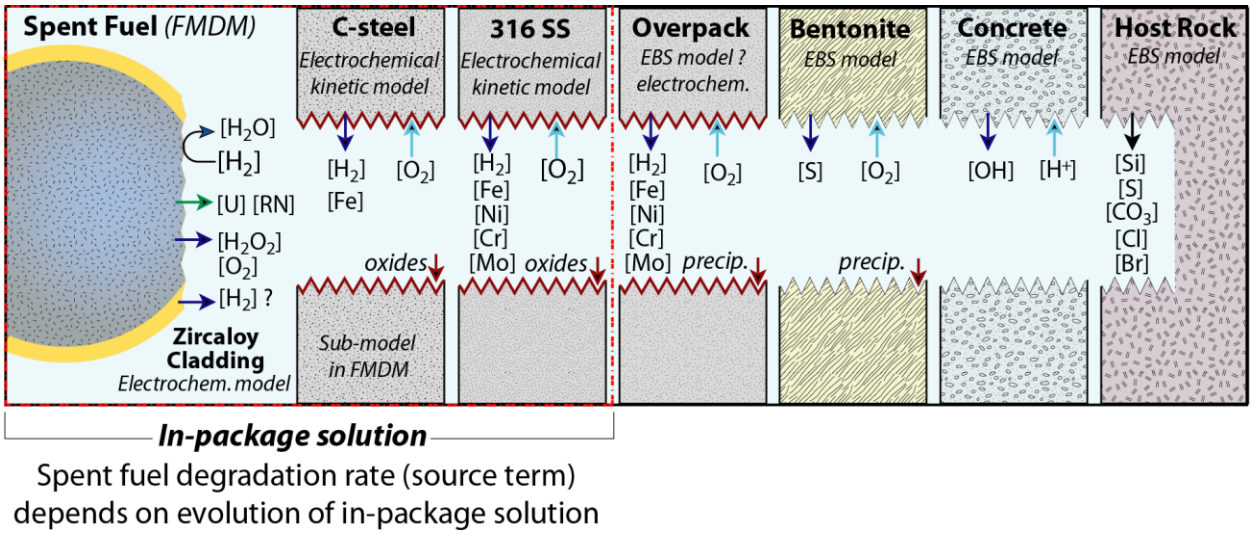

Figure 7. Schematic diagram depicting the interdependent chemical relationships between spent fuel, in-package alloy components and engineered barrier materials.

In addition to C-steel, 316 stainless steel and Zircaloy cladding, another important alloy that will be present in some spent fuel waste packages is the neutron absorbing material Boral™. Boral is a composite material consisting of aluminum plates ("cladding") enclosing a layer of boron carbide (B_4C). The B_4C grains, which range in diameter from approximately 0.01 to 0.1 mm, are dispersed in an aluminum matrix. An SEM image of a Boral electrode used in the electrochemical corrosion tests discussed in Section 3 is shown in Figure 8. Understanding the corrosion behavior of this material is important because it is a potentially important source of H_2 in the waste package and it plays a key role in mitigating criticality concerns.

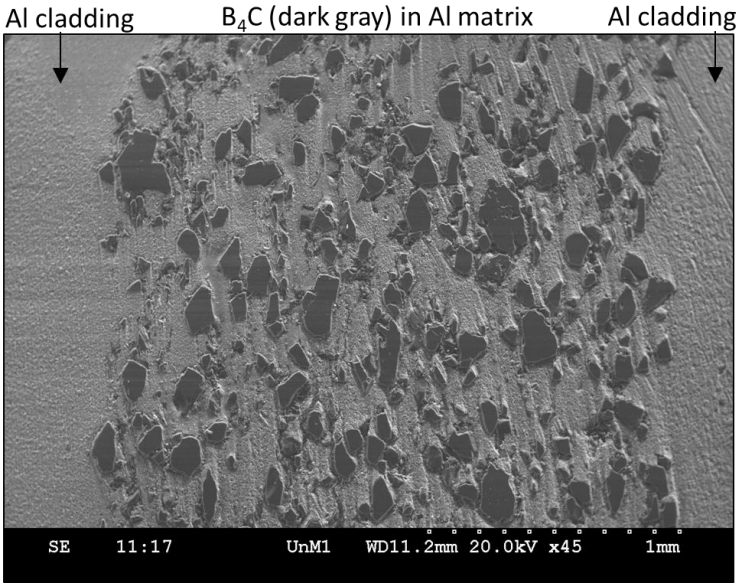

Figure 8. Scanning electron micrograph of Boral cross-section.

3. ELECTROCHEMICAL CORROSION EXPERIMENTS: KINETICS OF H_2 GENERATION

3.1. Background

Using accurate steel corrosion rates for relevant disposal conditions is essential for source term modeling because of the dominant effect of H_2 on the spent fuel dissolution rate (as discussed in Section 2 above). The half-cell reactions of particular interest for H_2 generation are as follows:

$Fe^0 \rightarrow Fe^{2+} + 2e^-$ (Reaction 1)

$2H_2O + 2e^- \rightarrow H_2 + 2OH^-$ (Reaction 2)
$2H^+ + 2e^- \rightarrow H_2$ (Reaction 3)

with the overall steel corrosion reactions

$Fe + 2H_2O \rightarrow H_2 + Fe^{2+} + 2OH^-$ (Reaction 4)
$Fe + 2H^+ \rightarrow H_2 + Fe^{2+}$ (Reaction 5)

Reactions 4 and 5 provide the fundamental coupling between steel corrosion and H_2 generation in acidic and neutral or alkaline solutions. (Analogous reactions can be written for aluminum corrosion to form $Al(OH)_3$ and Zircaloy corrosion to form ZrO_2.) The oxidation of other steel constituents (e.g., Cr, Mo, Ni, and Mn) will contribute to the anodic current, but the oxidation of Fe will be dominant. The threshold potential and reaction rates will depend on the surface potential imposed by the seepage water.

As discussed in Jerden et al., 2017, there is a wealth of literature on steel corrosion but much of the previous work was not done under repository-relevant conditions. Furthermore, the studies that were done using relevant solutions, such as bentonite pore waters (see reviews by Johnson and King, 2003 and King, 2007), involved batch style immersion tests that provide average cumulative rates rather than the instantaneous corrosion rates needed to parameterize and validate the FMD model.

Although Steel coupon immersion tests provide useful information on mineralogy and the evolution of the chemical system, corrosion rates derived from immersion tests are based on cumulative mass loss measurements or corrosion layer thicknesses that do not indicate how the corrosion rate (and thus H_2 generation rate) varies with time or conditions (most importantly, with the solution Eh). Knowing these dependencies of the H_2 generation rate is essential for modeling spent fuel dissolution under evolving in-package chemical conditions.

In an immersion test with a passivating steel, most of the mass loss occurs before the steel surface is passivated. The average rate may be relatively high, but the actual instantaneous rate that controls H_2 generation could have been high for a short initial interval but low for the majority of the test duration. We need to know how the instantaneous corrosion rate changes as the conditions evolve to accurately represent the flux of H_2 in the FMD model. Electrochemical techniques allow us to measure instantaneous rates under carefully controlled chemical and redox conditions. The difference between the cumulative rates from immersion tests and instantaneous rates measured with electrochemical methods is illustrated in Figure 9, where the blue curve shows the actual mass loss during a coupon corrosion test. At the end of the test duration the corroded coupon is weighed to determine the mass lost due to corrosion (blue circle, Figure 9). This method yields an average corrosion rate as indicated by the dashed green line in Figure 9. The majority of mass loss that occurred prior to passive stabilization dominates the cumulative mass loss and is

not well-represented by the average rate, which depends "artificially" on the test duration. That is, the average rate will decrease with longer test durations even though most of the mass loss occurred early in the test.

The instantaneous (kinetic) rate of corrosion (which gives the H_2 generation rate) that is given by the slope of the blue curve decreases significantly as the surface stabilizes and becomes much lower than the average cumulative rate. Whereas a series of immersion tests can be conducted for different durations to derive the mass loss curve, the method will not be sufficiently sensitive to measure the mass loss of a passivated surface. Perhaps more important from the modeling perspective, the immersion tests do not provide indications of the solution Eh or surface potential at which the steel is corroding and cannot be used to determine the dependence of the corrosion rate on the solution Eh. Immersion tests with actively corroding materials can only provide corrosion rates at the values of E_{corr} attained during the test, which will drift to unknown values during the test. The instantaneous rate that is measured directly as the corrosion current with electrochemical methods is needed to calculate the H_2 generation rate in the FMD model as a function of solution redox and chemistry. Electrochemical tests can be conducted to measure the corrosion rate at fixed potentials in solutions having known compositions.

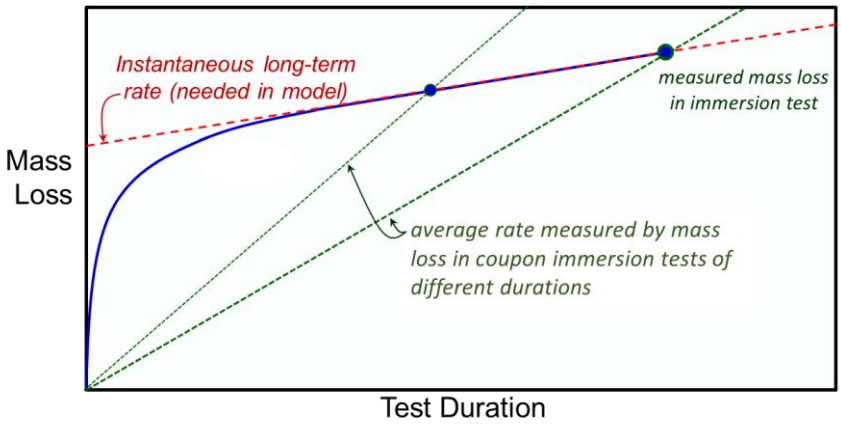

Figure 9. Conceptual diagram showing how mass loss measurements of steel corrosion rates in immersion tests yield rates that do not represent the corrosion kinetics (adapted from Jerden et al., 2017).

Electrochemical tests also quantify the effects of surface stabilization due to passivation and localized corrosion, such a pitting, that can only be qualitatively observed in coupon immersion tests. Furthermore, electrochemical methods can measure rates on the order of nanograms cm^{-2} d^{-1}. Therefore, the use of electrochemical methods provides reliable corrosion rates for durable EBS materials (including Zircaloy cladding) and provides dependencies on environmental conditions needed to predict the long-term generation of H_2 and attenuation of fuel degradation rates as the seepage water composition evolves.

3.2. Method and Results

The electrochemical corrosion experiments performed at Argonne employ the standard three electrode method as described by Bard and Faulkner, 2001. The three-electrode cell used for the Argonne tests consists of a 20 mL jacketed, borosilicate glass vessel with a mercury/mercurous Sulfate reference electrode, a graphite counter electrode and a carbon steel, 316L stainless steel, Zircaloy, aluminum alloy, or Boral working electrode. A typical electrochemical cell and working electrode is shown in Figure 10. Voltages have been adjusted to report relative to standard hydrogen electrode (SHE) for use in the FMD model.

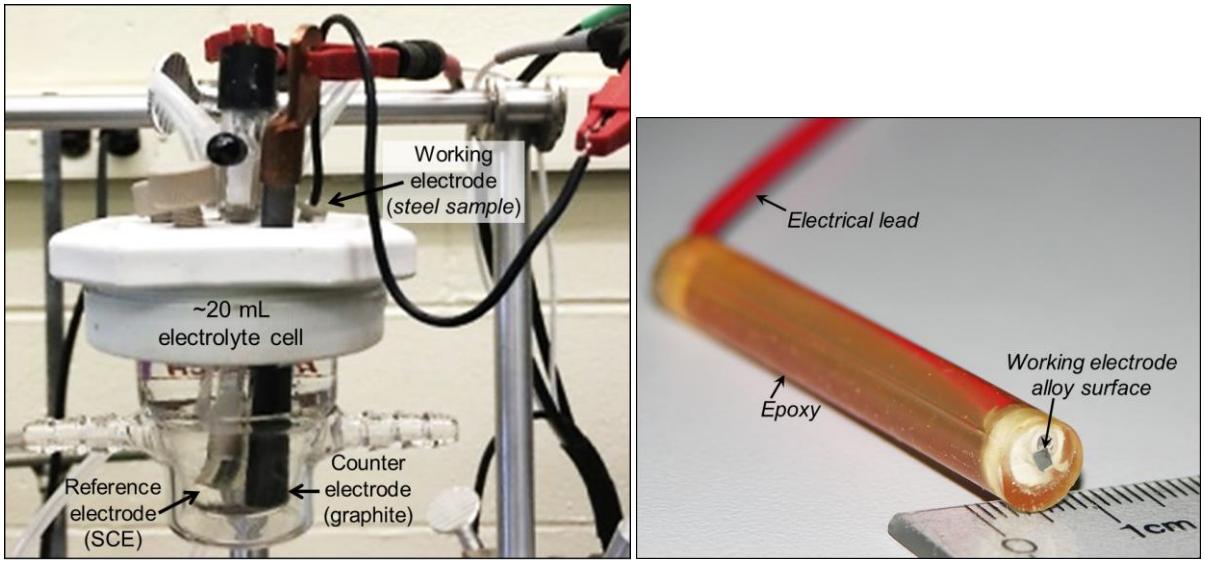

Figure 10. Three-electrode electrochemical cell used in Argonne electrochemical experiments (left) and an example alloy working electrode (right). The working electrode shown is made of Zircaloy-4, but the electrodes made with other materials are about the same size and mounted in the same way.

In the electrochemical tests, the electrolyte is used to impose chemical effects, including pH and Cl^- concentrations, and a potentiostat is used to impose a surface potential representing the solution Eh. The potentiostat can be used to impose a wide range of fixed potentials to efficiently determine the effect of the solution Eh on the steel corrosion and H_2 generation rate in the same chemical environment. In practice, a potentiodynamic scan is performed to measure E_{corr} for the polished surface in the test solution and identify regions of active and passive behavior to be studied in subsequent potentiostatic tests. The potentiodynamic scan indicates the propensity for active or passive corrosion, but the rapid scan rate does not allow stable passive layers to form. Potentiostatic tests are conducted to measure the corrosion currents as stable passive layers form or the constant currents that are achieved with actively corroding metals.

The stabilized current densities measured in the potentiostatic test are converted directly into alloy corrosion rates using Faraday's Law. Faraday's Law relates the cumulative charge transferred through the working electrode to the mass of metal oxidized during an experiment (Equation 1). Since the cumulative charge transferred is a function of the reaction current over time (Equation 2) we can use current densities measured during potentiostatic tests to calculate corrosion rates (Equations 3 and 4)

$$m = \frac{QM}{nF}$$ Equation 1

where m is the mass of substance oxidized, Q is the total electric charge passed through the electrode substance, M is the molecular weight of the electrode substance, F is the Faraday constant, and n is the number of electrons transferred.

The cumulative electric charge Q is the integrated reaction current measured at the electrode:

$$Q = \int_0^t I(t)\, dt \qquad \text{Equation 2}$$

Where $I(t)$ is the reaction current measured at the electrode at time t. Therefore, the mass of material oxidized at the electrode surface can also be calculated from the measured reaction current at the electrode. If the corrosion current is constant, the mass corroded over an interval Δt can be calculated as:

$$m = \frac{I \cdot \Delta t\, M}{nF} \qquad \text{Equation 3}$$

and the rate can be calculated as

$$rate = \frac{m}{\Delta t} = \frac{I\, M}{n\, F}\,. \qquad \text{Equation 4}$$

The current and mass released can be normalized to the surface area of the electrode to give corrosion rates in units of g m^{-2} yr^{-1}, which can be converted to penetration rates in mm yr^{-1} using the density of the steel. It also gives the H_2 generation rate using the stoichiometry of Reactions 4 and 5 shown above.

Each electrochemical experiment involves the following sequence of steps:

- electrochemical cleaning at a potential far below the corrosion potential of the material to remove any native oxide from the sample electrode.
- potentiodynamic scans to determine E_{corr} of alloy under chemical conditions of interest,
- potentiostatic holds at several relevant redox conditions,
- electrical impedance spectroscopy at the potentiostatic voltage to characterize the properties of passivating oxide layers,
- detailed microscopy (reflected light, SEM/EDS) to characterize alloy microstructures before and after corrosion tests.

The results from these tests provide the following information:

- corrosion rates for stabilized surfaces formed under controlled environmental conditions,
- electrical properties of the passivated surfaces to provide confidence in their long-term stability,
- analytical expressions for key dependencies (Eh, pH, T, chloride concentration) to formulate rate laws to calculate H_2 generation rates in the FMD model for the corrosion of different materials.
- corrosion products for further analyses

The parametric conditions used for the tests discussed in this report are as follows:

- Potentiodynamic polarization tests
    - *Alloys*: 316L-SS, C-steel (AISI 4320), Zircaloy-4, Boral, Al-1100
    - pH: 4, 7, 10 (in Fischer pH buffers)

  - NaCl concentrations: 0, 4, 100 millimolar.
  - Potential swept from around -550 mV_{SHE} up to around 1.7 V_{SHE}
- Potentiostatic polarization tests
  - *Alloys*: 316L-SS, C-steel (AISI 4320), Zircaloy-4
  - pH: 4, 7, 10 (in Fischer pH buffers)
  - NaCl concentrations: 4 millimolar.
  - Constant potential: 494 mV_{SHE}

Figure 11 shows potentiodynamic data for 316 stainless steel. The results indicate passive corrosion over the full potential range for tests in solutions with no NaCl and with 4mM NaCl. The 100 mM NaCl tests show a breakdown in passivation at different potentials depending on the pH. For the pH 4 test, the passivation breakdown occurs at a potential around 0.55 V_{SHE} while at pH 7 the breakdown occurs near 0.9 V_{SHE} and at pH 10 around 0.85 V_{SHE}.

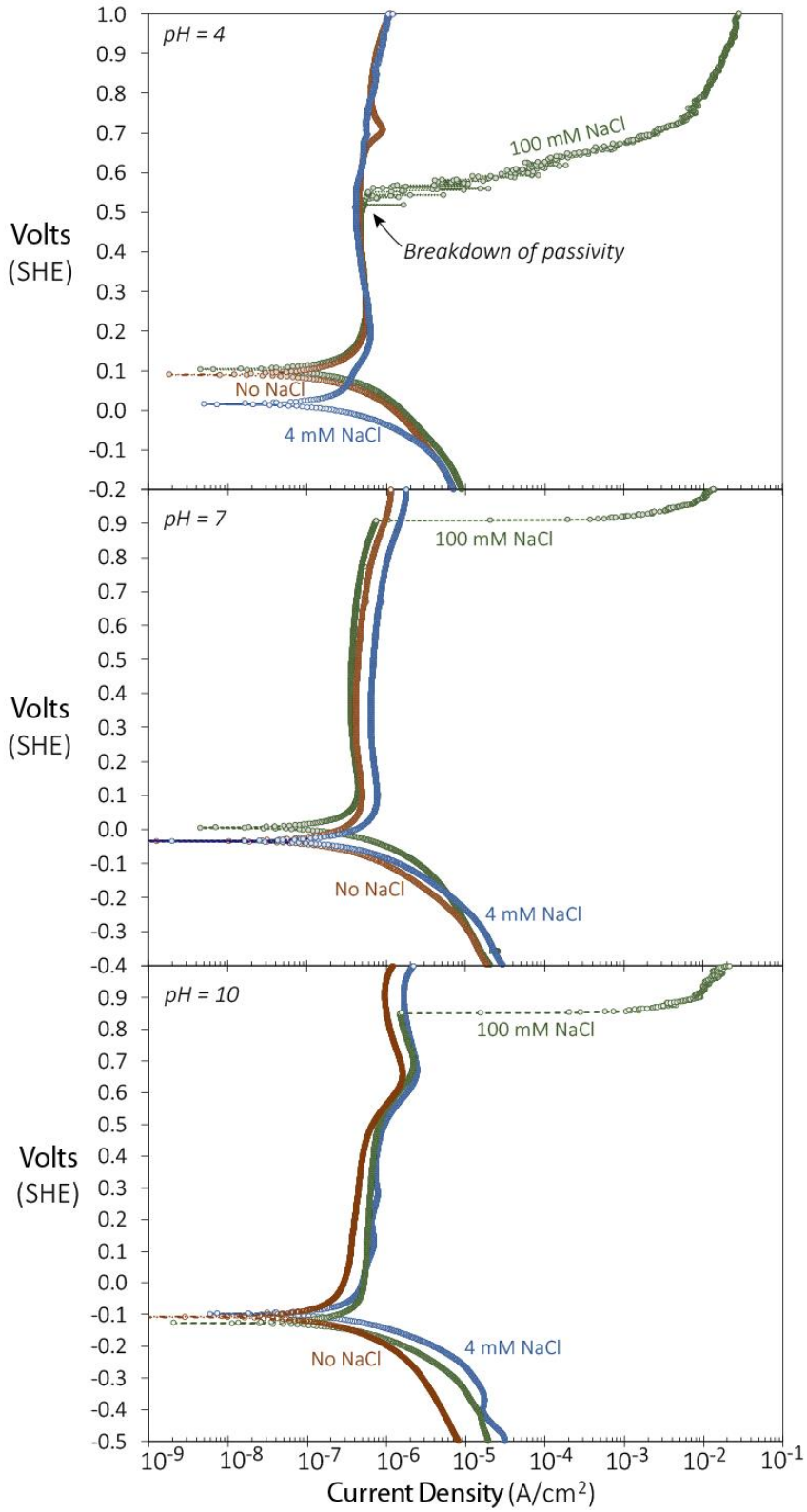

Figure 11. Potentiodynamic polarization data for 316 stainless steel for pH 4, 7 and 10 solutions with 0, 4 and 100 mM NaCl shown by the red, blue, and green curves, respectively.

Figure 12 shows the potentiostatic data for 316 SS at a held potential of 494 V_{SHE} with in 4mM NaCl for the three pH values. The low current densities indicate passive corrosion rates on the order of 0.2 – 0.5 µm/yr (based on Faraday's law). The gaps indicate when electrochemical impedance spectroscopy (EIS) analyses were performed and the current was not measured. The EIS results for the tests discussed in this report are undergoing analyses and interpretation and will presented in a future report. The "thickness" of the curves reflects the dynamic balance between the anodic and cathodic reactions occurring on the electrode surface. The higher values are used to represent the alloy corrosion rates.

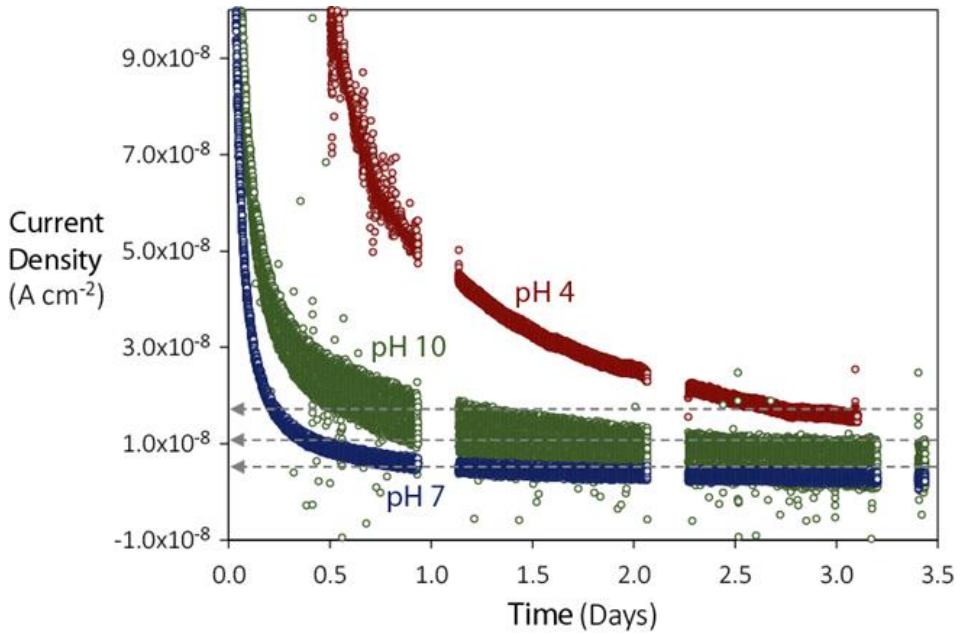

Figure 12. Potentiostatic test results for 316 SS for pH 4, 7, and 10.

Figure 13 show results from the potentiodynamic polarization tests for carbon steel (AISI 4320). The pH 4 results (top plot) indicate active corrosion in solutions with and without added chloride concentrations. For the pH 7 test, the formation of an oxide layer (magnetite) slows corrosion by blocking the surface thus slowing the cathodic reactions (Reactions 2 and 3 above). In the 4 mM NaCl solution, the effect of this oxide layer is removed at a potential of around 0.4 V_{SHE}, leading to active corrosion. In the 100 mM NaCl test, the breakdown of the oxide layer effect occurs at a potential around 0.3 V_{SHE}.

In the pH 10 solutions, the scans show multiple corrosion potentials (E_{corr} values). These current density minima correspond to phase transitions within the oxide layers forming on the steel surfaces. The lowest E_{corr} corresponds to the transition from a ferrous hydroxide to magnetite and the Ecorr around -0.35 V_{SHE} corresponds to the transition from magnetite to ferric hydroxide (goethite or ferrihydrite). The E_{corr} between 0 and 0.1 V_{SHE} is the corrosion potential of the alloy surface at pH 10. In the 100 mM solution, the ferric hydroxide layer breaks down around a potential of 0.1 V_{SHE}, whereas in the 4 mM NaCl test the oxide layer breaks down at around 0.6 V_{SHE}.

The correlations between the current density minima and phase transitions in the oxide layer are demonstrated in Figure 14.

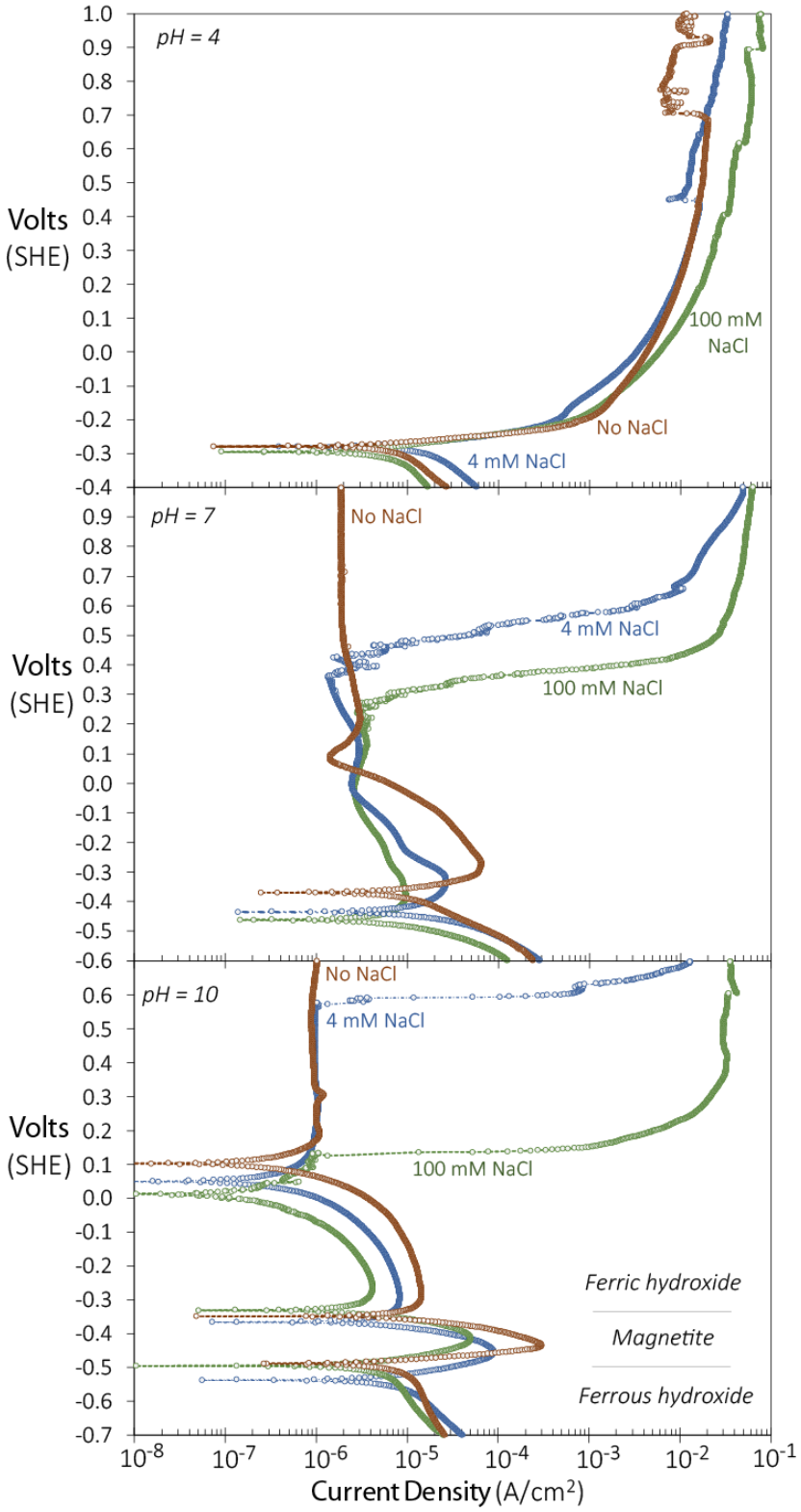

Figure 13. Potentiodynamic polarization results for carbon steel (AISI 4320).

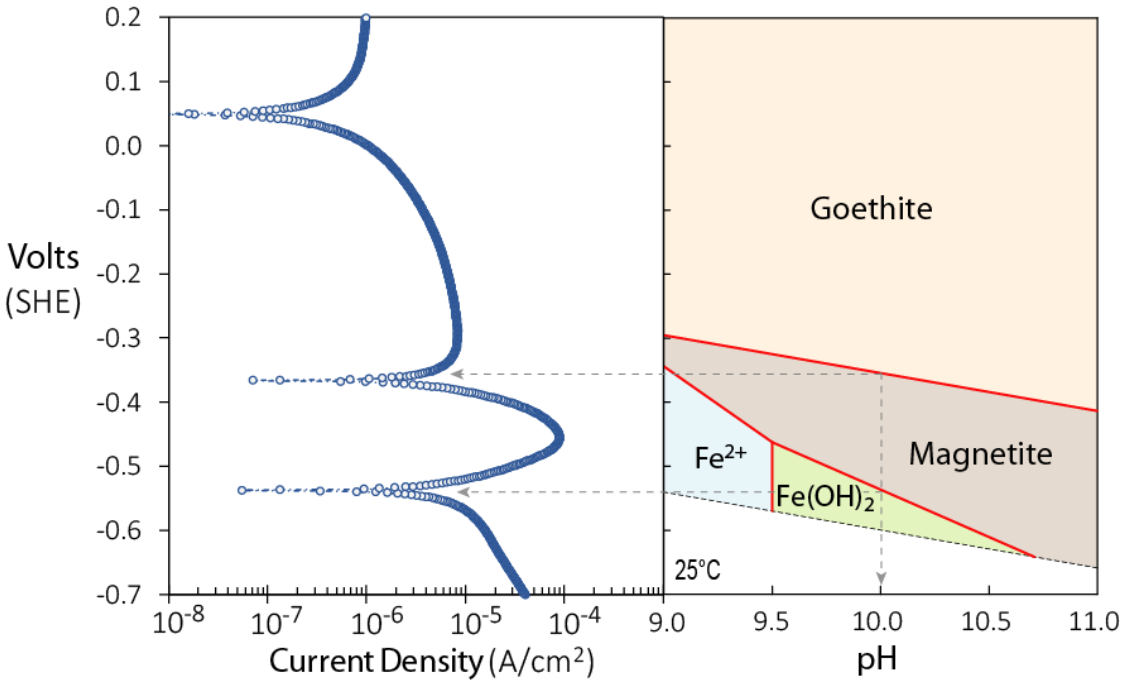

Figure 14. Pourbaix diagram for 10^{-7} iron and the potentiodynamic data from the pH 10 test with no NaCl.

Potentiostatic tests were performed on the C-steel electrode at pH 4, 7 and 10 in 4mM NaCl, at 494 mV_{SHE} to determine the stable (instantaneous) corrosion rate. Results from these potentiostatic polarization tests are shown in Figure 15 indicate rapid corrosion at all pH values. The current densities shown in Figure 15 correspond to corrosion rates on the order of millimeters per year based on Faraday's law.

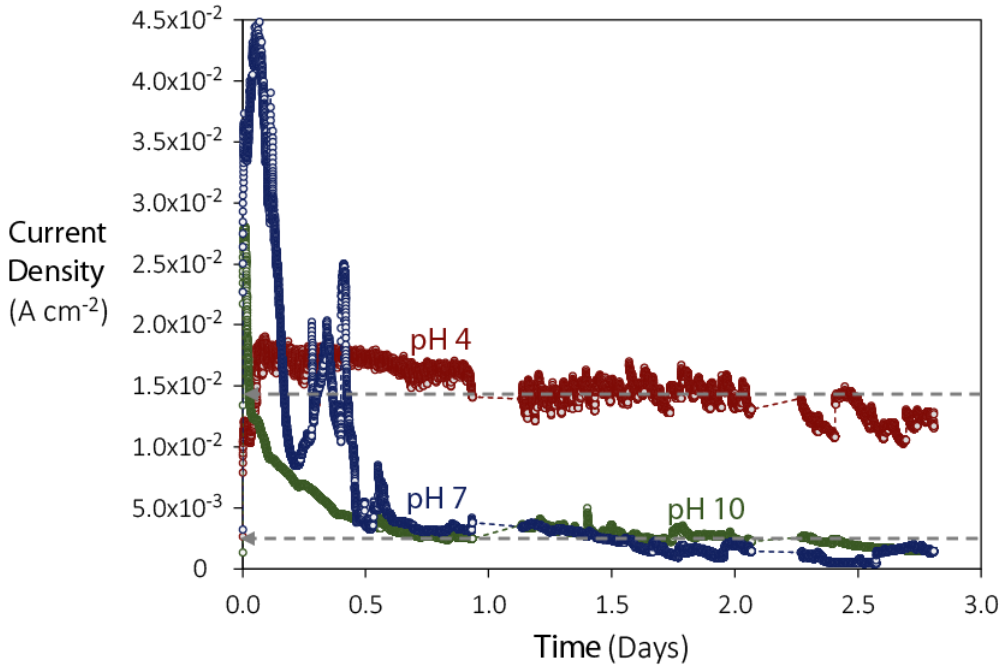

Figure 15. Potentiostatic polarization tests for carbon steel (AISI 4320) at 250 mVSCE.

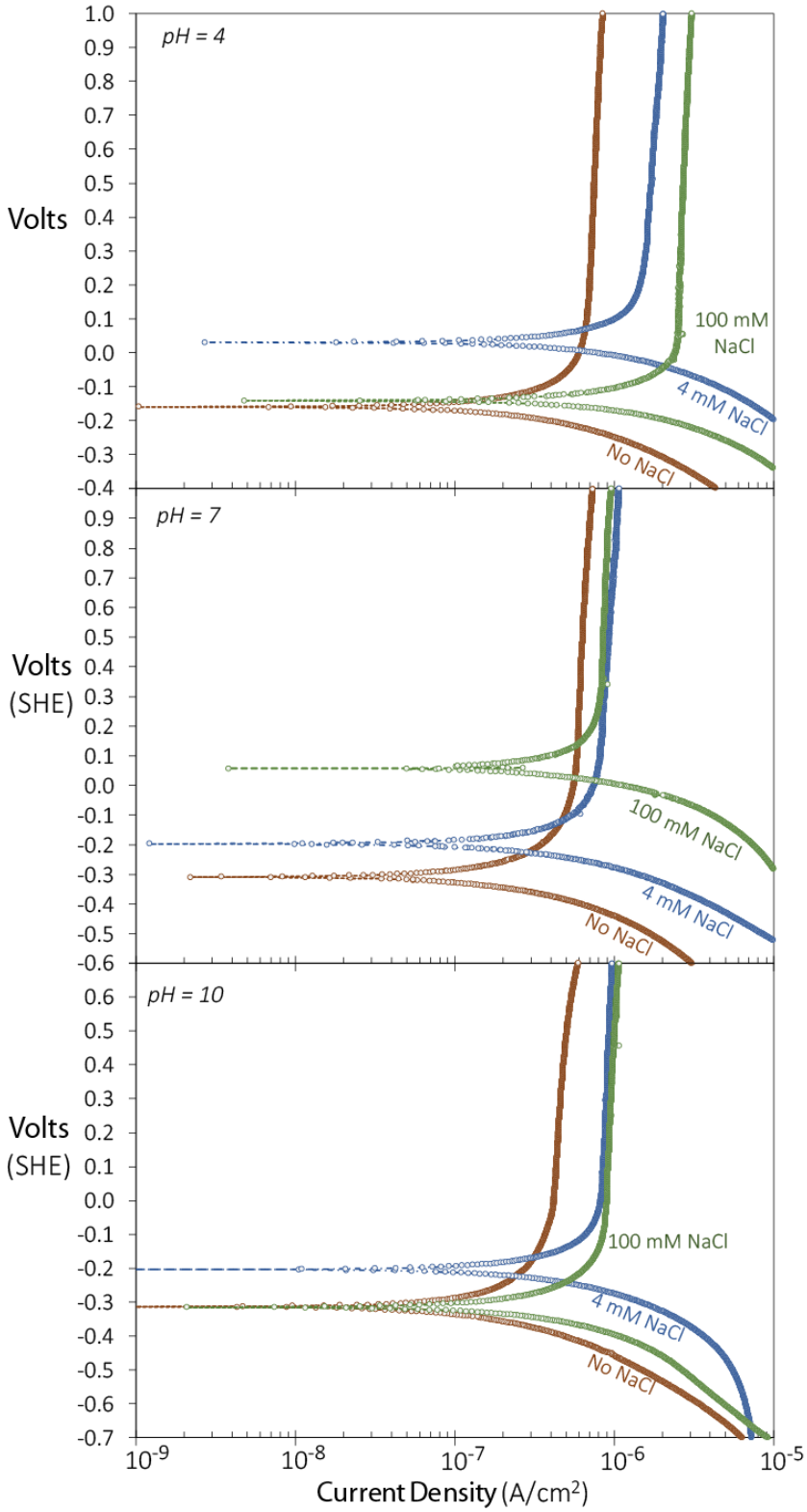

Figure 16. Potentiodynamic tests for Zircaloy 4.

Results from potentiodynamic tests on Zircaloy-4 (Figure 16) show passive corrosion over the entire range of potentials, pH and chloride concentrations. This behavior is due to the formation and persistence of a zirconium oxide corrosion layer throughout the tests. The Zircaloy-4 potentiostatic test results (Figure 17) show nanoamp to sub-nanoamp current densities indicating corrosion rates of less than 1.0 μm/year (based on Faraday's law) for the tests in pH 4 and pH 7 solutions and less than 2 μm/year for the test performed at pH 10.

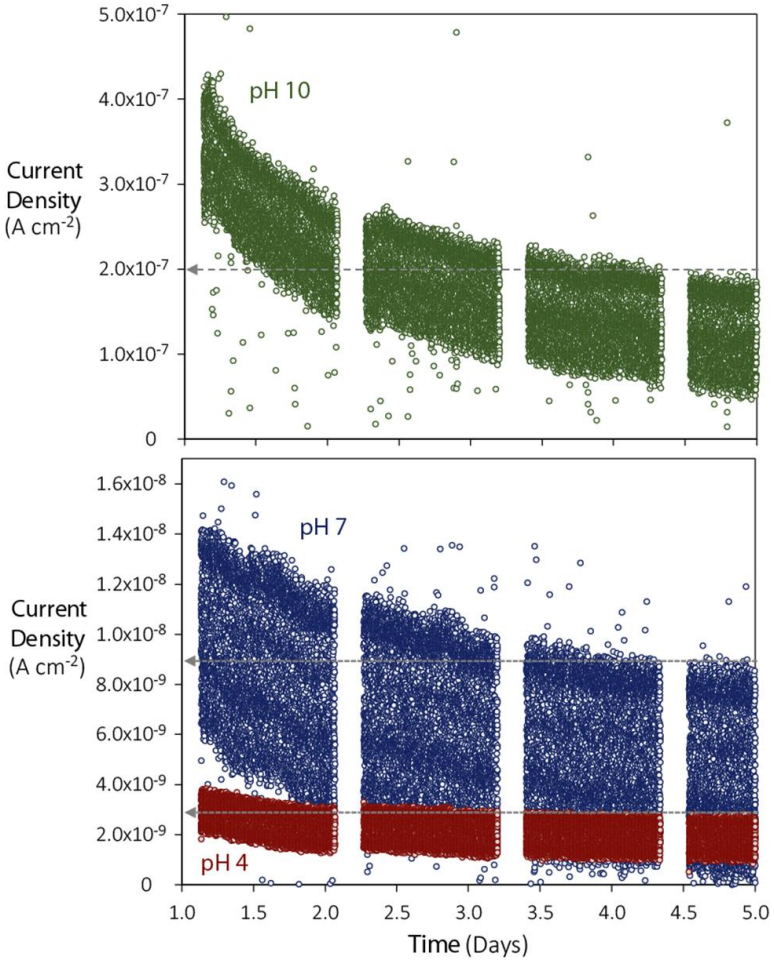

Figure 17. Potentiostatic polarization test results for Zircaloy-4 at 250 mVSCE in 4 mM NaCl solutions adjusted to pH 4, 7, or 10.

The potentiodynamic corrosion test data for Boral and pure aluminum (Al-1100) are shown in Figure 18. The top plot in Figure 18 is for an electrode containing both the aluminum cladding plates and the aluminum/boron carbide particle composite (see Figure 8 above). The middle plot is from a test with an electrode consisting only of the boron carbide composite. The results indicate rapid, active corrosion of both materials at pH 4 and 7. In the pH 10 solution, the current densities are relatively high (~0.3 milliamp/m^2) but are still approximately a factor of 30 lower than in tests in the pH 4 and 7 solutions at potentials lower than 0 volts. The lower current density for the pH 10 test is due to the formation of an aluminum hydroxide corrosion phase that partially blocks the metal surface from rapidly exchanging electrons with the solution. Above a potential of around 0 volts, the hydroxide phase evidently becomes less effective at protecting the metal surface, as the current densities begin to increase for the pH 10 tests above this potential.

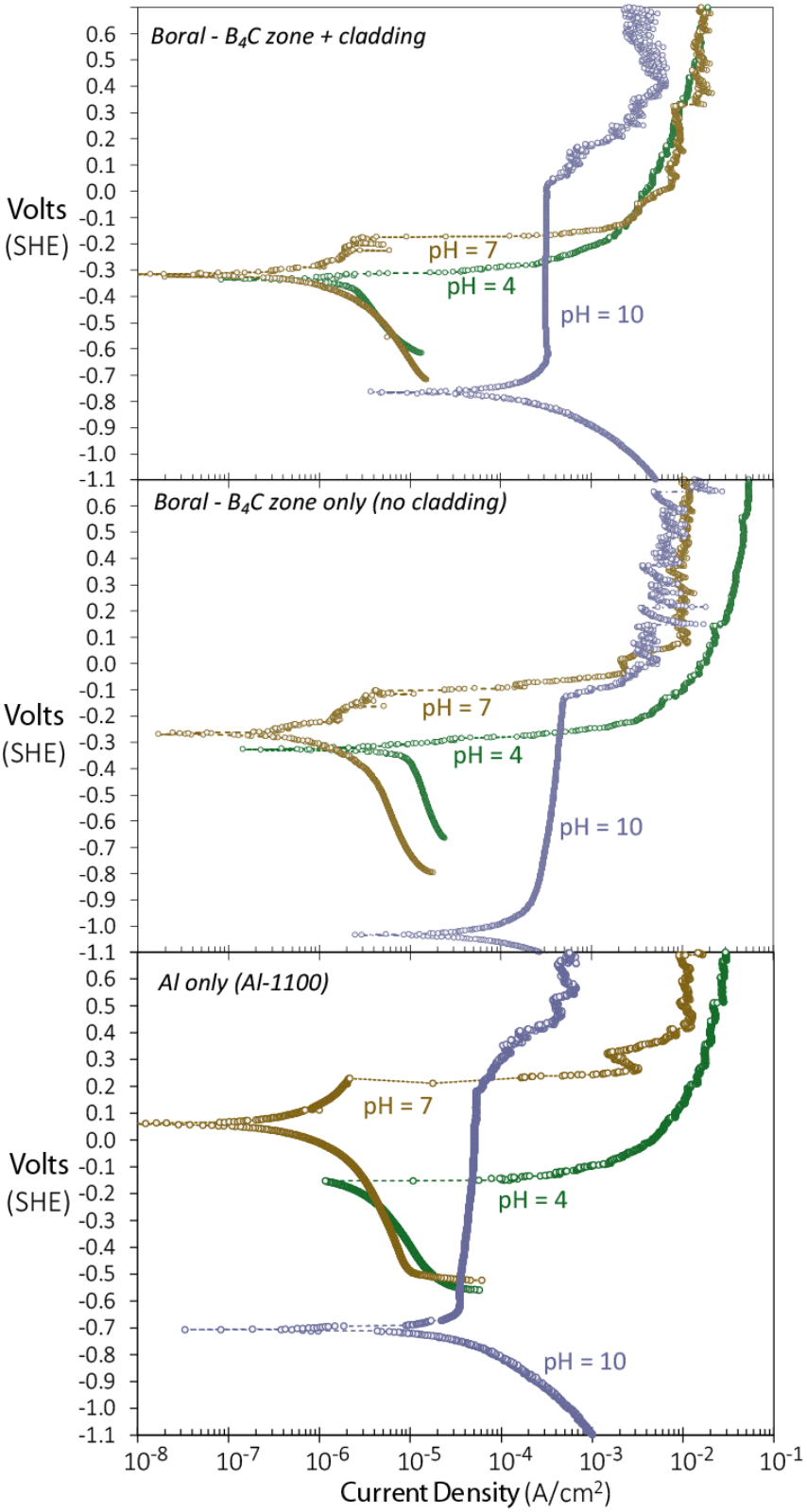

Figure 18. Potentiodynamic polarization test results for Boral and pure aluminum-1100 in 4 mM NaCl.

The bottom plot in Figure 18 shows the potentiodynamic scan for pure Al-1100. The results show the same trends as the Boral samples but indicate a more effective surface protection at pH 10, where current densities are over two orders of magnitude lower than the pH 4 and 7 samples.

Figure 19 shows SEM micrographs of the corroded electrodes of Boral from the potentiodynamic tests shown in the top plot of Figure 18. The microscopy indicates that the samples in pH 4 and pH 7 solutions corroded by uniform removal of both the aluminum matrix within the B_4C zone as well as the surrounding aluminum cladding material. The B_4C particles appear to be resistant to corrosion but are physically released as the surrounding aluminum matrix corrodes. The pH 10 sample (Figure 19(d)) shows the aluminum matrix to be preferentially corroded thus exposing the B_4C particles. The texture of the aluminum surrounding the B_4C zone suggests that the metal surface is coated with an aluminum hydroxide layer.

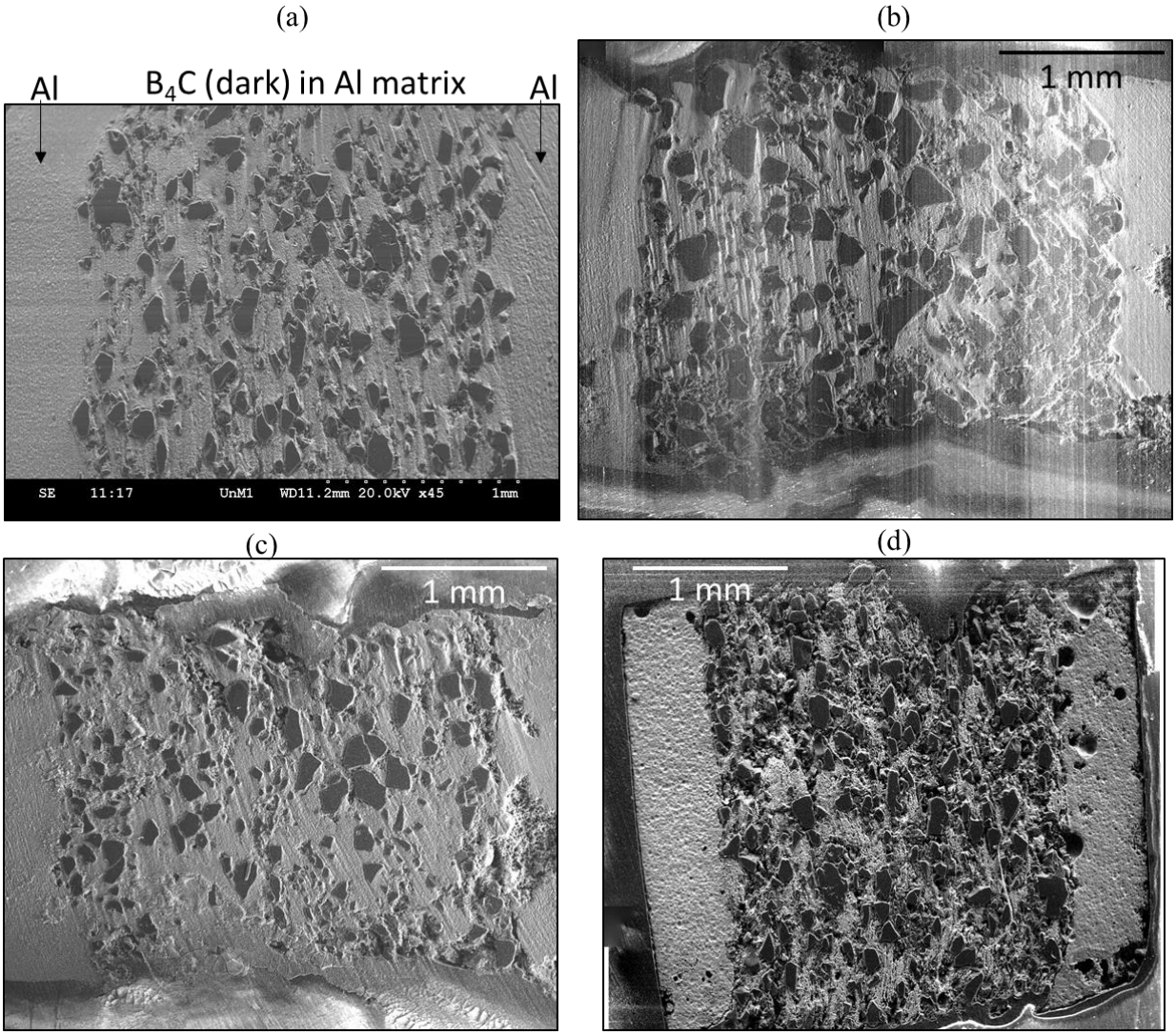

Figure 19. Boral electrodes before and after potentiodynamic scans: (a) is the pre-corroded electrode surface, (b) is from the pH 4, potentiodynamic test, (c) is from the pH 7 potentiodynamic test and (d) is from the pH 10 potentiodynamic test.

Table 1. summarizes the corrosion rates measured from the potentiostatic tests discussed above. The results shown in Table 1 are used as inputs for the FMD model sensitivity runs discussed in the Section 4 below.

Table 1. Summary of corrosion rates from potentiostatic tests at 494 mV_{SHE} in 4.0 millimolar NaCl.

	Current density (A/cm^2)			Corrosion Rate (um/yr)			Corrosion Rate (g /m^2 yr)		
	pH 4	pH 7	pH 10	pH 4	pH 7	pH 10	pH 4	pH 7	pH 10
316L-SS	$1.6x10^{-8}$	$4.4x10^{-9}$	$1.0x10^{-8}$	0.19	0.05	0.12	1.48	0.41	0.92
4320 C-steel	$1.4x10^{-2}$	$1.4x10^{-3}$	$2.2x10^{-3}$	$1.4x10^{5}$	$1.6x10^{4}$	$2.6x10^{4}$	$1.1x10^{6}$	$1.3x10^{5}$	$2.1x10^{5}$
Zircaloy-4	$3.1x10^{-9}$	$9.0x10^{-9}$	$2.2x10^{-7}$	0.04	0.11	1.89	0.28	0.83	14.91

As shown in Figure 20, there is no consistent trend between corrosion rate and pH in potentiostatic test results. For example, the 316L stainless steel sample corrodes at similar rates in the pH 4 and pH 10 solutions, but the rate in the pH 7 solution is approximately a factor of 3 lower than the other two tests. The corrosion rate for C-steel is around a factor of 10 higher in the pH 4 solution vs the pH 7 solution; however results from the test at pH 10 yields a slightly higher rate than the test at pH 7. The Zircaoly-4 corrosion rates generally increase with increasing pH, however, more data are needed to confirm if there is a true functional dependence as the results from the tests performed at pH 4 and pH 7 only differ by 0.07 micrometers per year.

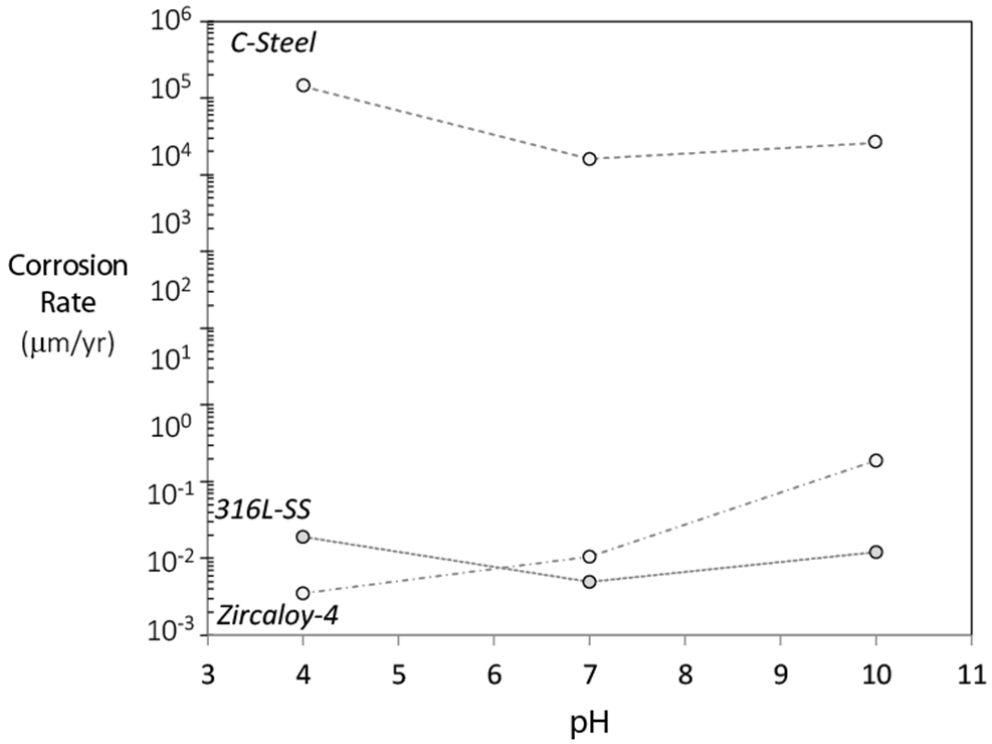

Figure 20. Corrosion rate vs pH plot from potentiostatic test data shown in Table 1 above. All tests were run at 494 mV_{SHE} in 4.0 millimolar NaCl.

4. IN-PACKAGE CHEMISTRY SIMULATION AND THE FUEL MATRIX DEGREDATION MODEL: ROLE OF ALLOY CORROSION

The reaction-path modeling code Gechemist's Workbench (GWB) (Bethke, 2014) was used with the FMD model to investigate how the H_2 concentration may evolve as the metal alloy components and spent fuel within a failed canister all corrode simultaneously. The modeling approach builds on that described used in Jerden et al., 2017.

The thermodynamic database used for this model was thermo.com.V8.R6 (Johnson et al, 2000) to which the steel reactants were added. The masses of the different steel components, their surface areas, and total solution volume were those given in the in-package chemistry model used for the YM TSPA (CRWMS, 2003). The alloy masses used for this model are shown in Table 2, and the initial groundwater composition, which is typical of a crystalline rock repository environment, is shown in Table 3. The volume of solution used in the model was 4.1 m^3, which is based on the void volume within the spent fuel canister assumed in CRWMS, 2003.

Table 2. Values used in the base-case Geochemist's Workbench in-package model (from CRWMS, 2003).

Materials	**Total Mass** (kg)	**Specific Surface Area** (m^2 g^{-1})
316 SS	$5.9x10^3$	$4.1x10^{-6}$
C-steel	$1.2x10^3$	$8.7x10^{-5}$
Al-6061	190	$2.8x10^{-4}$

Table 3. Initial solution composition used in Geochemist's Workbench in-package model (from Fernandez et al., 2007). This composition is typical pore-water from the Opalinus clay.

Component	**Concentration** (molar)
pH	7.4
Na	$2.8x10^{-1}$
Ca	$2.3x10^{-2}$
K	$2.2x10^{-3}$
Mg	$2.1x10^{-2}$
Fe	$3.5x10^{-6}$
Cl^-	$3.3x10^{-1}$
SO_4^{2-}	$1.9x10^{-2}$
CO_3^{3-}	$5.2x10^{-3}$
SiO_2	$1.1x10^{-4}$

The GWB in-package model was expanded from the simple titration model used in Jerden et al. 2017 by adding a 1-D reactive transport model using the X1t code. The layout and discretization of the model is shown schematically in Figure 21. The model includes 21 reaction/diffusion cells with the central cell including the materials shown in Table 2 (i.e. the waste package cell). The diffusion coefficient used for H_2 in all model cases was $6.0x10^{-5}$ cm^2/s (Turnbull, 2008). The porosity of the waste package cell was set to 80%, while the porosity in the bentonite and host rock cells (see Figure 21) were set to 30%.

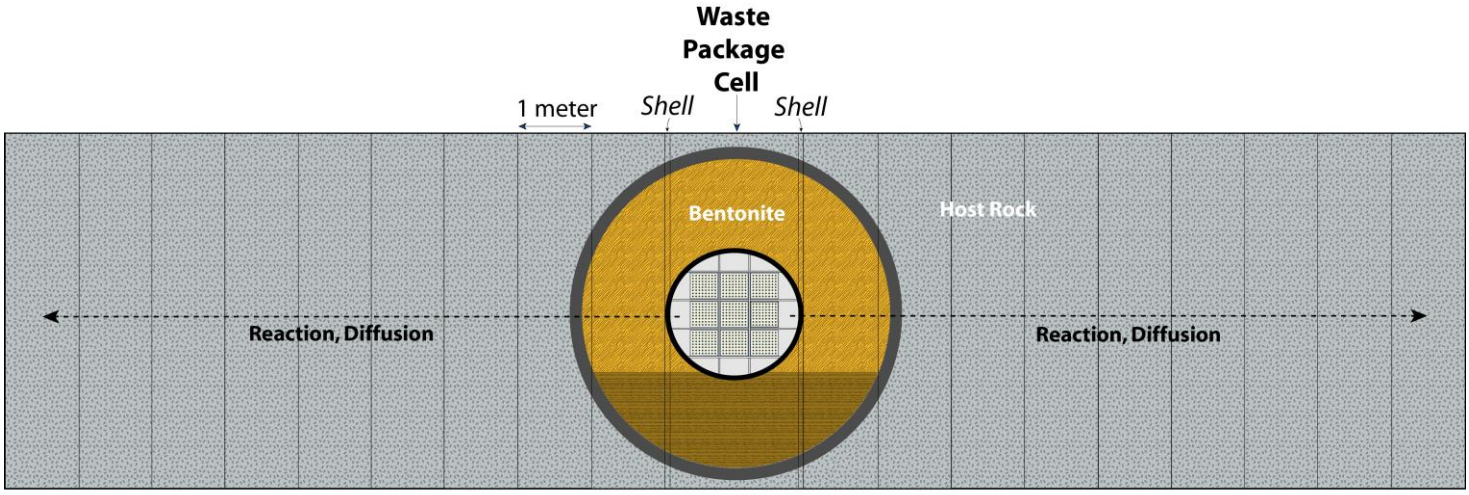

Figure 21. Schematic layout of the GWB in-package model used to calculate the dissolved concentration of H_2 within a generic breached waste package over a 10^5 year repository scenario.

The four main functions of the GWB in-package model are:

- To determine the amount of H_2 produced and accumulated over a range of relevant alloy corrosion rates.
- To quantify the kinetics of H_2 removal (by diffusion or advection) from the waste package cell containing the spent fuel.
- To track the dissolved H_2 concentration within the in-package solution based on the first two bullets.
- Provide the H_2 concentration as a function of time to the FMD model so that the spent fuel degradation rate can be calculated as the in-package environment evolves.

The GWB in-package model discussed in this section represents a "first-pass" or scoping model for quantifying in-package H_2 concentrations while accounting for diffusive and advective transport. other important structural components (i.e., other alloys) present within the EBS are not yet included in the model. These other components will be added to the model after this initial model version has been tested and assessed. Later iterations of the model can include cell (medium) specific diffusion and advection rates (e.g., to simulate a pin-hole breach in the canister) and processes that could consume H_2, such as reactions with sulfur and microbial activity.

The conditions for the sensitivity runs performed with this combined GWB-FMD model are shown in Table 4.

Table 4. Conditions for sensitivity runs performed using the GWB-FMD model discussed in this report.

	4320 C-Steel (g m^{-2} yr^{-1})	Source of Rate	316 SS (g m^{-2} yr^{-1})	Source of Rate	Al-6061 (g m^{-2} yr^{-1})	Source of Rate	Advection through waste package (m/yr)
Case 1	$1x10^5$	This study	0.3	This study	1180	This study[1]	0 *(diffusion only)*[3]
Case 2	$1x10^5$	This study	0.3	This study	1180	This study[1]	0.1
Case 3	312	CRWMS, 2003	0.3	This study	590	This study[2]	0 *(diffusion only)*[3]
Case 4	312	CRWMS, 2003	0.3	This study	590	This study[2]	0.1
Case 5	312	CRWMS, 2003	0.3	This study	1180	This study[1]	0 *(diffusion only)*[3]

[1]This is an estimate made from the potentiodynamic data ($4x10^{-5}$ amp/m^2, from Figure 17, Al-1100 plot] as the potentiostatic tests have not yet been completed.
[2]This is a factor of 2 lower than the estimated case 1 and case 2 value, it is a placeholder used for the sensitivity calculations.
[3]The diffusion coefficient used of H_2 in all model runs was $1.0x10^{-5}$ cm^2/s.

Each model run involved the following steps:

- The initial condition of the reactive transport domain (Figure 21):
  - All cells fully saturated with a solution of the composition shown in Table 3.
  - The model starts with the condition of a breached and fully saturated waste package.
  - The spent fuel is assumed to be contacted by the in-package solution.
- The age of the fuel is assumed to be 1100 years out of reactor. Therefore, the model assumes that the waste package failed and was filled with solution 1000 years after emplacement and that the fuel was 100 years out of reactor when it was emplaced.
- The three alloys (Table 2) are congruently reacted with the solution composition given in Table 3 at the rates specified in Table 4.
- Geochemist's Workbench was used to determine the evolution of the pH, Eh and speciation (solution and solids) of the simulated in-package solution corresponding to a given set of steel dissolution rates.
- The amount of H_2 produced and its distribution with time over the reactive transport domain (through diffusion and advection) are determined and quantified as fugacity and molal concentrations (e.g., Figures 22 and 23).
- Results from the in-package solution simulations (i.e. H_2 concentrations) are used as input to the FMD model, which is then used to calculate the spent fuel degradation rate.
  - Parameter values for the fuel environment are from Jerden et al., 2015.
  - Temperature was held constant at 25 ^oC for all runs.
  - Each model case included two fuel burnup values (40 GWd/MTU and 80 GWd/MTU) as indicated in the results (Figure 22 - 31).

Figure 22 shows the fugacity of H_2 generated due to alloy corrosion across the reactive/transport domain (see Figure 21) as a function of distance and time for model Case 1 (Table 4). The waste package domain is located at the center of the diagram (~9 m). The numbers on the plot indicate the number of years elapsed since the initiation of alloy corrosion within the waste package. For case 1 the rapid peak in H_2 fugacity is due to the initially rapid corrosion of C-steel, which is nearly completely consumed within 20 years of the start of corrosion.

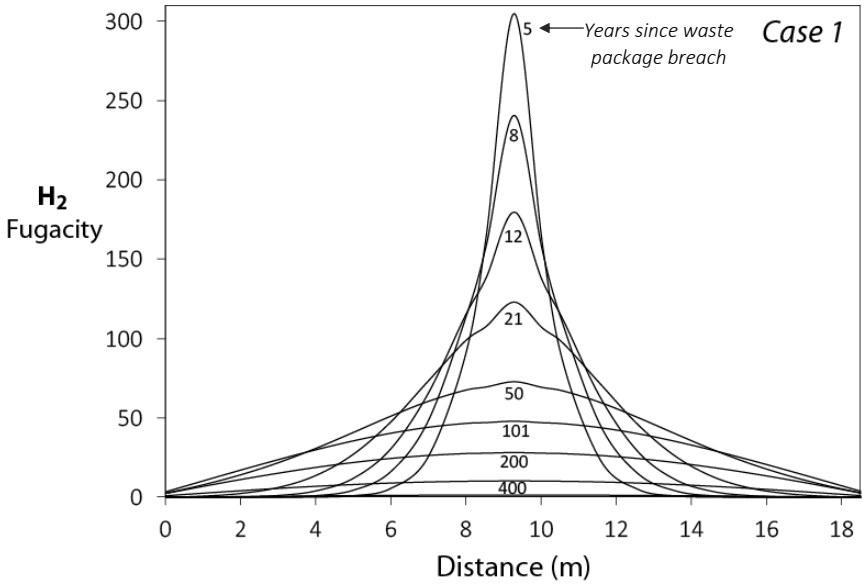

Figure 22. Hydrogen fugacity vs. distance and time predicted by the GWB in-package model for Case 1 (Table 4). The numbers shown adjacent to the fugacity curves are the number of years since alloy corrosion started.

Figure 22 shows that, for the high measured alloy corrosion rates used in for Case 1 (Table 4), the H_2 fugacity has risen from near zero to 300 just 5 years after the initiation of corrosion within the waste package. The fugacity decreases relatively rapidly over the first 50 years due to H_2 diffusion into the EBS and near-field. By year 400 the H_2 fugacity has decreased to less than 10 within the waste package.

As shown in Figure 23(a), the rapid increase in H_2 is due primarily, to the rapid corrosion of C-steel, which is nearly consumed within 20 years of the initiation of corrosion. The main source of H_2 following the degradation of C-steel is the aluminum alloy (Al-6061) which is consumed within 100 years of corrosion initiation. As shown in Figure 23(b), the concentration of H_2 does not immediately decrease after the consumption of both C-steel and Al-6061. This is due to the diffusion limited transport of H_2 away from the waste package and the persistent generation of H_2 by the slowly corroding 316 stainless steel. The corrosion of 316L keeps the H_2 concentration well above the threshold value of approximately 0.1 mM H_2 needed to inhibit the oxidative dissolution of spent fuel [Figure 23(c)]. The alternative, no H_2 cases shown as dotted lines in Figure 23(c) indicate that, the presence of anoxically corroding alloys suppress the spent fuel dissolution rate by over 3 orders of magnitude over the duration of the model.

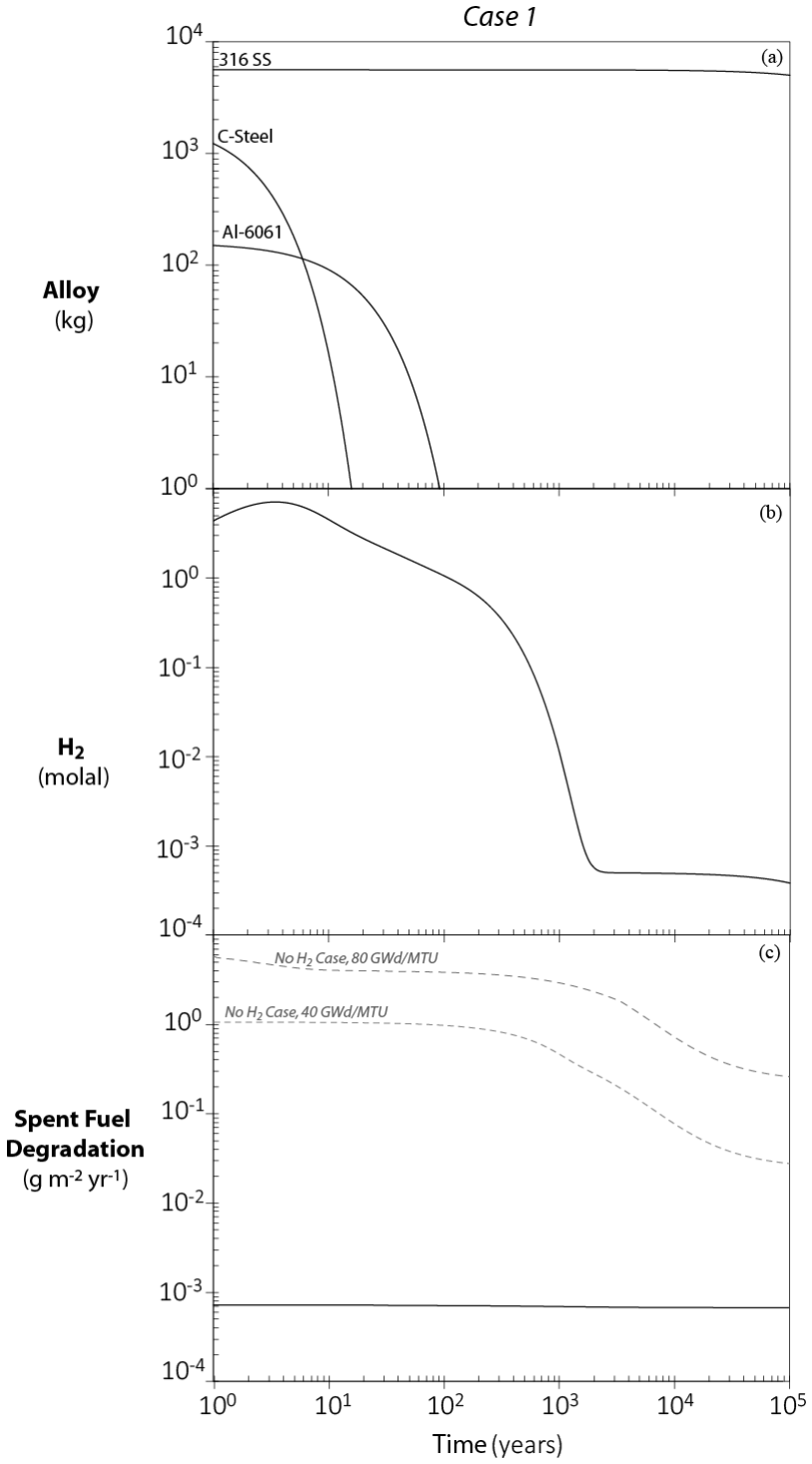

Figure 23. Results from Case 1 model scenario (Table 4). The time axis refers to the time elapsed from the start of in-package corrosion (assumed to be 1000 years after emplacement). The fuel is assumed to be 1100 years old at time zero in these model runs. The dotted lines in the bottom plot show the degradation rates calculated for cases with no H_2 for a high burnup fuel (80 GWd/MTU) and a moderate burnup fuel (40 GWd/MTU). The solid line below 10^{-3} g/m^2 yr is the calculated degradation rate for the Case 1 scenario.

Figure 24 shows the H_2 fugacity vs time plot for Case 2, which includes a slow advection rate of 0.1 m/yr through the waste package (the in-package solution moves from left to right, Figure 24). The rapid alloy corrosion rates again cause a rapid increase in H_2 fugacity within the first few years of corrosion. This is followed by a rapid decrease due to both diffusion and advection. The advective transport of H_2 out of the waste package is indicated by the asymmetric profile that becomes prominent in year 14.

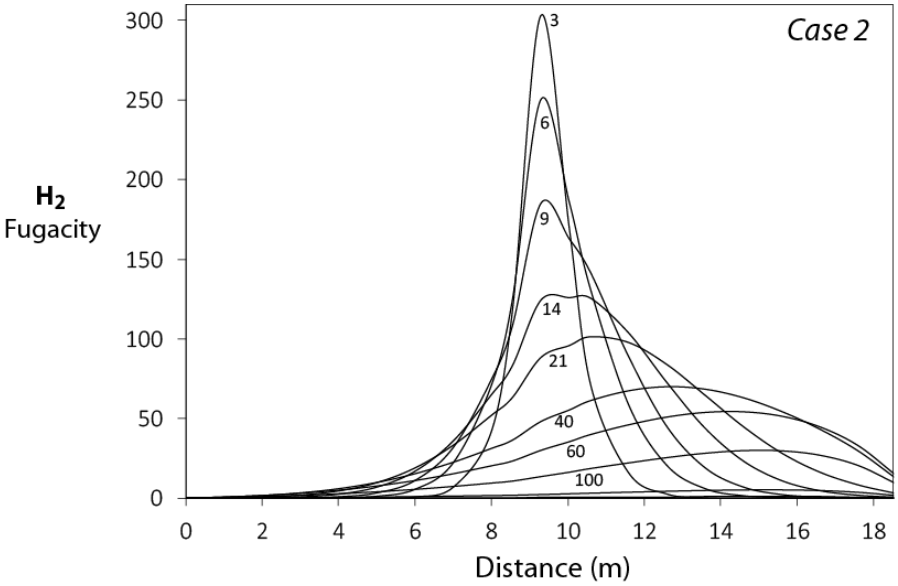

Figure 24. Hydrogen fugacity vs. distance and time predicted by the GWB in-package model Case 2 (Table 4). The numbers shown adjacent to the fugacity curves are the number of years since alloy corrosion started. The waste package domain is located at the center of the diagram (~9 m).

The decrease in alloy mass with time shown in Figure 25(a) is the same as the Case 1 run because the same alloy corrosion rates are used. However, the predicted H_2 concentration with time [Figure 25(b)] is quite different from Case 1 due to the advective transport of H_2. As H_2 is continuously swept out of the waste package, the H_2 concentrations drop rapidly following the consumption of the rapidly corroding C-steel and Al-6061. In this case, the continuous slow corrosion of 316 SS does not generate enough H_2 to maintain the dissolved concentration required to inhibit the oxidative dissolution of the fuel. As shown in Figure 25(c), the FMD model predicts that once the dissolved concentration of H_2 falls below 10^{-5} molal, the spent fuel dissolution rates will increase to values that would be expected if no H_2 was present. For the Case 2 conditions this fuel degradation rate increase is predicted to occur around 600 years after corrosion started.

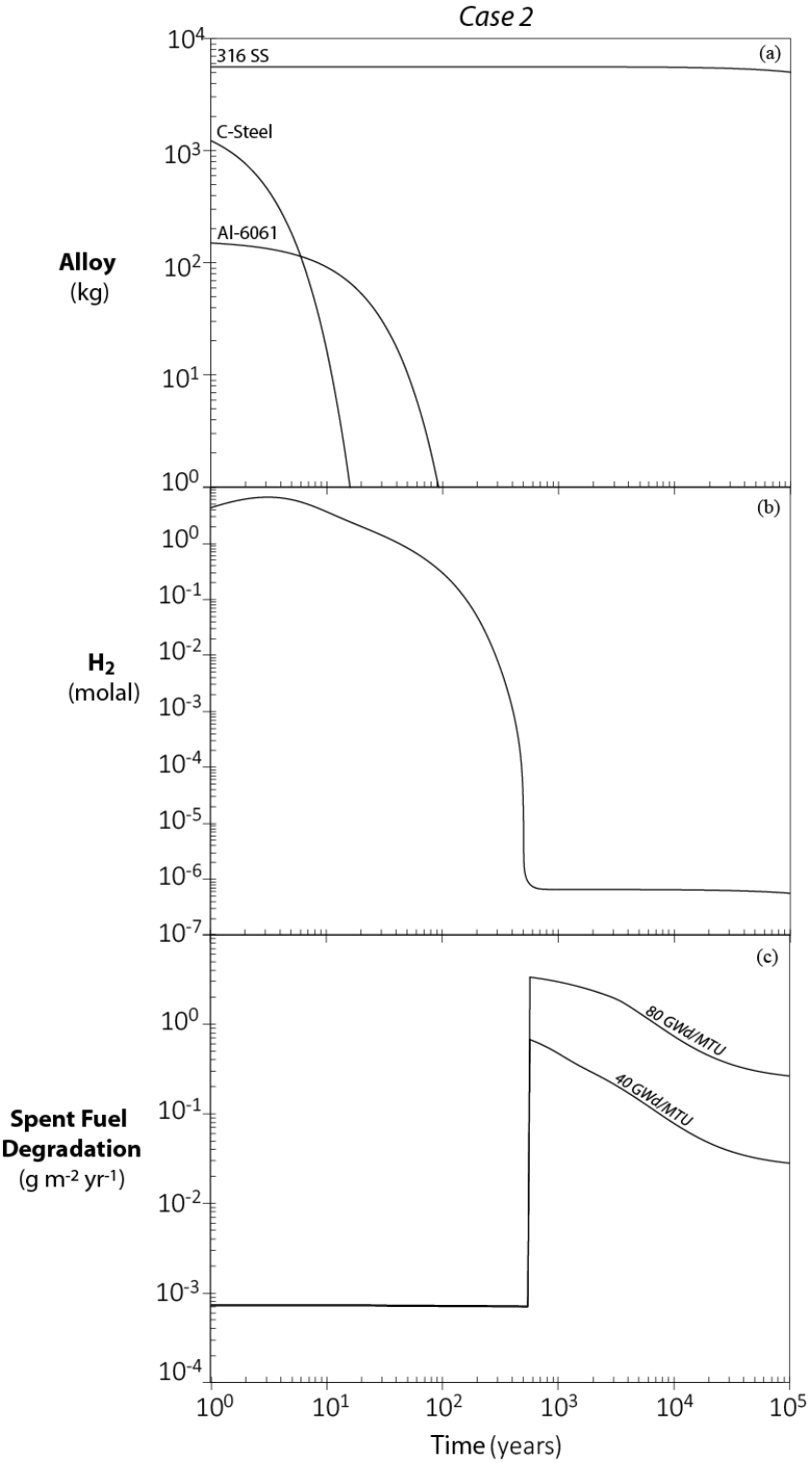

Figure 25. Results from Case 2 model scenario (Table 4). The time axis refers to the time elapsed from the start of in-package corrosion (assumed to be 1000 years after emplacement). The fuel is assumed to be 1100 years old at time zero in these model runs.

Figure 26 shows the H_2 fugacity vs time plot for Case 3, where the slower corrosion rates for C-steel and Al-6061 are used (Table 4). This results in significantly lower peak H_2 fugacity (~80 for Case 3 vs ~300 for Case 1) and a slower overall decrease in H_2 fugacity within the waste package reaction cell.

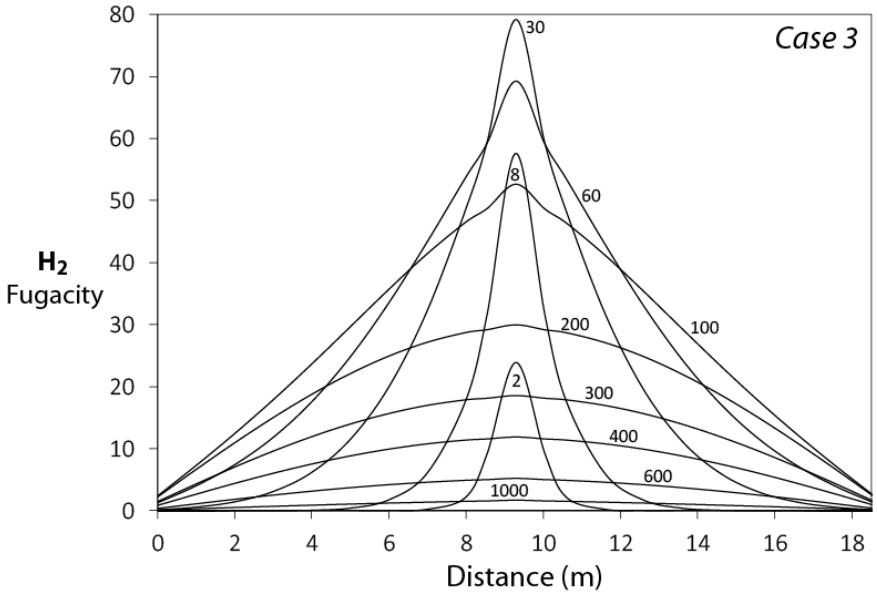

Figure 26. Hydrogen fugacity vs. distance and time predicted by the GWB in-package model Case 3 (Table 4). The numbers shown adjacent to the fugacity curves are the number of years since alloy corrosion started. The waste package domain is located at the center of the diagram (~9 m).

As shown in Figure 27(a) the Case 3 alloy corrosion rates result in C-steel lasting for around 300 years and Al-6061 lasting for around 7000 years. This results in a relatively high H_2 concentration for nearly 10,000 years. As shown in Figure 27(c), for this scenario with no advective transport, the slow corrosion of 316 SS generates enough H_2 to keep the dissolved concentration above the threshold needed to suppress oxidative dissolution of the fuel (~0.1 mM H_2).

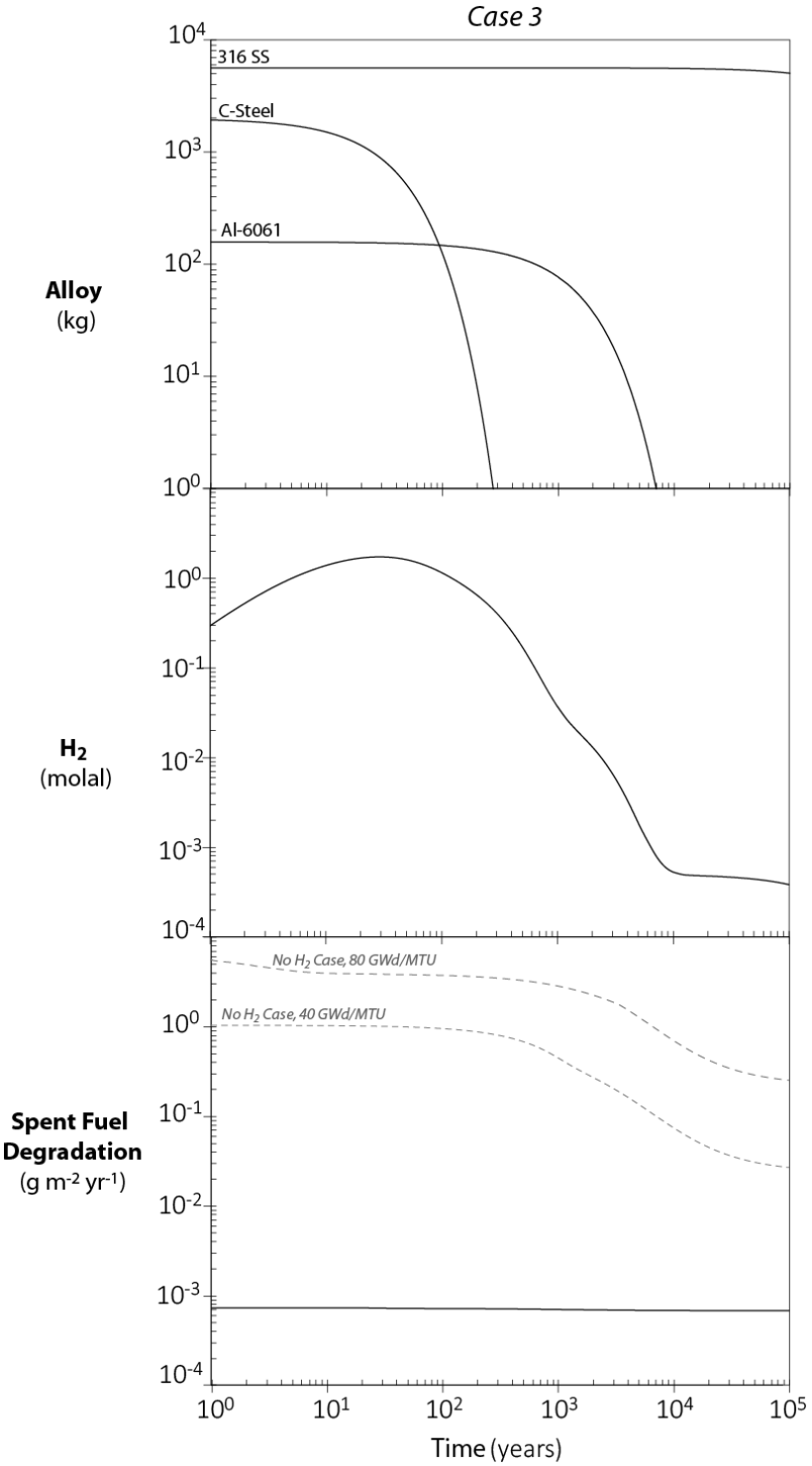

Figure 27. Results from Case 3 model scenario (Table 4). The time axis refers to the time elapsed from the start of in-package corrosion (assumed to be 1000 years after emplacement). The fuel is assumed to be 1100 years old at time zero in these model runs. The dotted lines show the degradation rates calculated for cases with no H_2 for a high burnup fuel (80 GWd/MTU) and a moderate burnup fuel (40 GWd/MTU). The solid line below 10^{-3} g/m^2 yr is the calculated degradation rate for the Case 3 scenario.

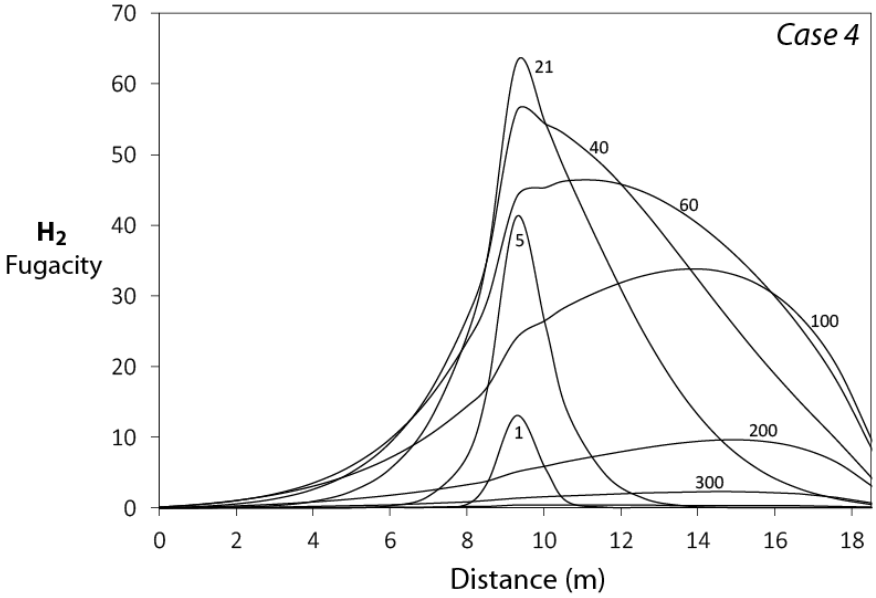

Figure 28. Hydrogen fugacity vs. distance and time predicted by the GWB in-package model Case 4 (Table 4). The numbers shown adjacent to the fugacity curves are the number of years since alloy corrosion started. The waste package domain is located at the center of the diagram (~9 m).

Figure 28 shows the H_2 fugacity vs distance plot for Case 4, which uses the same alloy corrosion rates as Case 3, but includes the advective transport of solution through the waste package at a rate of 0.1 m/yr. As indicated by the asymmetric H_2 profiles in Figure 28, the advection of solution causes a relatively rapid decrease in H_2 fugacity within the waste package cell. The alloy masses with time for Case 4 (Figure 29(a)) are the same as the Case 3 plot. however, due to the advective transport of H_2, the dissolved concentration falls below the threshold concentration needed to inhibit oxidative degradation of the fuel. As shown in Figure 29(c) the fuel degradation rates increase at 7000 years to values that would be expected if no H_2 was present.

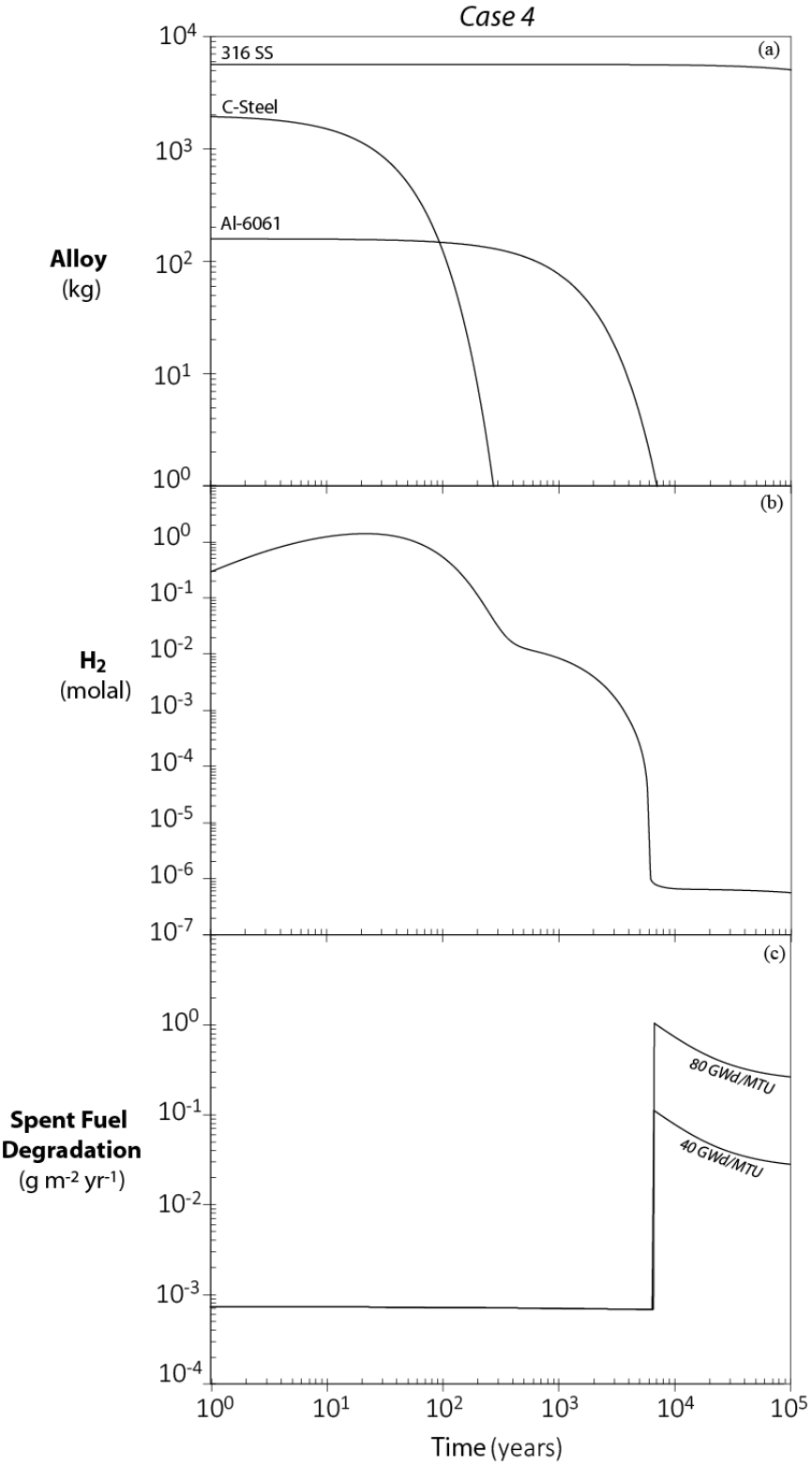

Figure 29. Results from Case 4 model scenario (Table 4). The time axis refers to the time elapsed from the start of in-package corrosion (assumed to be 1000 years after emplacement). The fuel is assumed to be 1100 years old at time zero in these model runs.

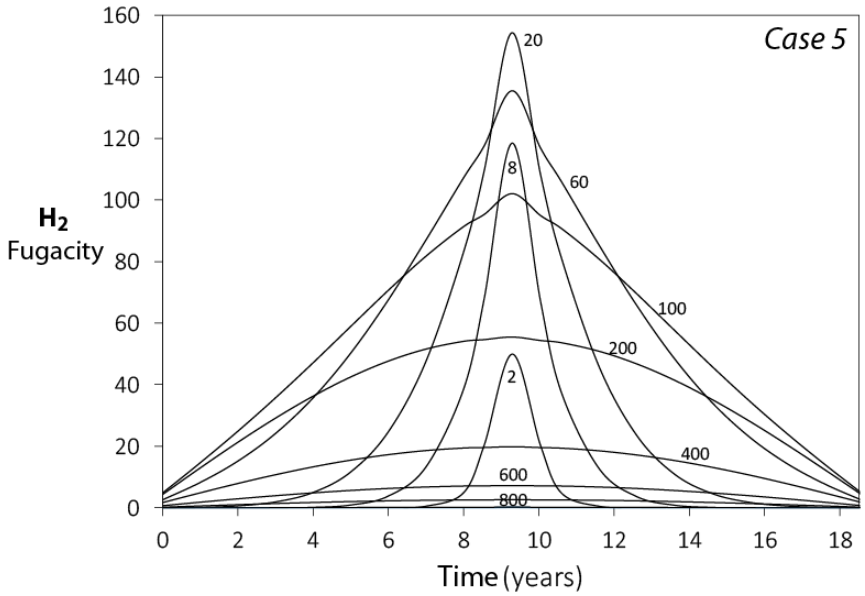

Figure 30. Hydrogen fugacity vs. distance and time predicted by the GWB in-package model Case 5 (Table 4). The numbers shown adjacent to the fugacity curves are the number of years since alloy corrosion started. The waste package domain is located at the center of the diagram (~9 m).

Figure 30 shows the H_2 fugacity vs distance results for Case 5 (Table 4). For this case, a relatively low corrosion rate is used for C-steel and a relatively rapid rate is used for Al-1100. Case 5 is further differentiated from Cases 1 – 4 by the assumption that there is more C-steel than 316 SS in the waste package [see Figure 31(a)]. With the relatively slow C-steel corrosion rate, it takes 20 years before the peak H_2 fugacity is reached and this is followed by the relatively long slow decrease in H_2 within the waste package cell (transport is only by diffusion in this case).

As shown in Figure 31(a) it takes 200 years for the C-steel to be consumed and the H_2 concentration remains relatively high (>0.1 mM) for 2000 years. Around the 2000 year mark the dissolved concentration of H_2 decreases to around 0.05mM. This is a high enough H_2 concentration to suppress the oxidative dissolution of fuel with a burnup of 40 GWd/MTU, but it is not high enough to fully suppress the oxidative dissolution of fuel with a burnup of 80 GWd/MTU [Figure 31(c)]. However, the increase in the fuel degradation rate around 2000 years is not significant because the slowly corroding 316 SS continues to supply H_2 to the system. The decrease in H_2 observed at around 40,000 years is due to the lower mass of 316 SS used for this case. By this time, enough 316 SS has been consumed to cause a significant decrease in H_2 generation.

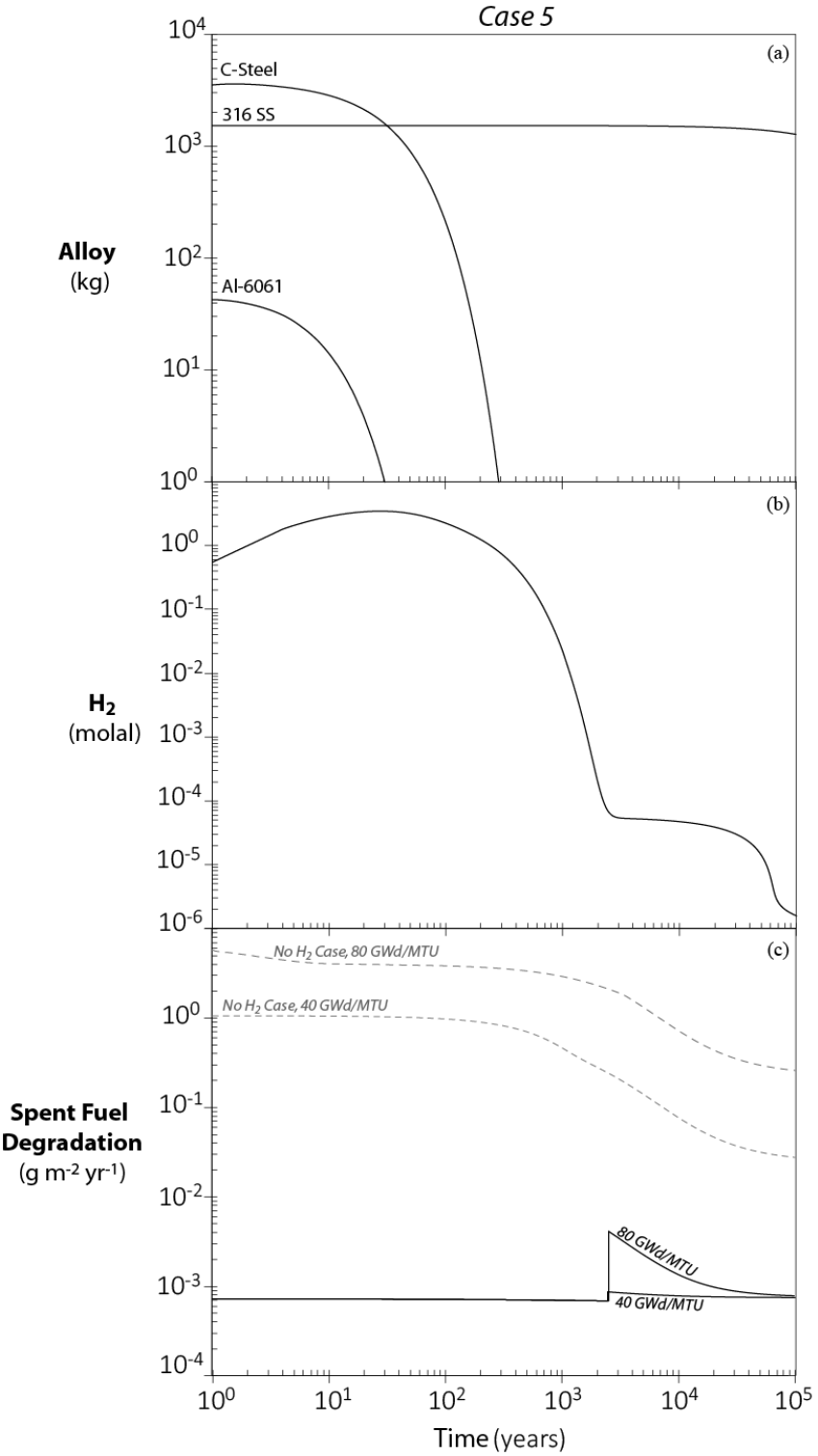

Figure 31. Results from Case 5 model scenario (Table 4). The time axis refers to the time elapsed from the start of in-package corrosion (assumed to be 1000 years after emplacement). The fuel is assumed to be 1100 years old at time zero in these model runs. The dotted lines show the degradation rates calculated for cases with no H_2 for a high burnup fuel (80 GWd/MTU) and a moderate burnup fuel (40 GWd/MTU). The solid line below 10^{-3} g/m^2 yr is the calculated degradation rate for the Case 5 scenario.

5. CONCLUSIONS AND FUTURE WORK

The purpose of this study is to develop and test a process model for the degradation of uranium oxide spent fuel that is based on fundamental thermodynamics, kinetics, and electrochemistry that can be directly integrated into a repository performance assessment model. Because the model is based on fundamental principles, it can be applied with confidence over geologic time scales and over a range of host rock and near-field environments (clay/shale or crystalline repository concepts). The main features of the fuel matrix degradation (FMD) model discussed in this report are summarized in Figure 3 above. The recent and on-going work described in Jerden et al., 2017, Jerden et al., 2018 and this report involved quantifying the role of H_2 that is produced from the anoxic corrosion of steels in suppressing oxidative dissolution of the fuel. To this end, an electrokinetic mixed potential model for steel corrosion was added to the FMD model to calculate the amounts of H_2 generated as various metallic components in a waste package corrode. Sensitivity calculations relating the fuel degradation rate to the steel corrosion rates were performed to identify information gaps that need to be addressed to fully couple, calibrate, and validate the models.

Specifically, this report presents results from a series of electrochemical corrosion tests that provide information needed to parameterize the FMD model. The alloys tested include 316L stainless steel (316SS), AISI 4320 carbon steel (C-steel), Zircaloy-4 fuel cladding (unirradiated) and a borated aluminum composite material (Boral). Potentiostatic and potentiodynamic polarization tests were performed in buffer solutions at pH 4, 7 and 10 with NaCl concentrations of 0, 4 and 100 millimolar (mM). All tests were performed at laboratory ambient temperatures (~22°C). These electrochemical tests provide new insights into the corrosion behavior of these key alloys. The primary findings are as follows:

The general insights gained from the electrochemical experiments are as follows:

- None of the alloys tested showed a correlation between corrosion rate and pH (Figure 20).
- Both 316L stainless steel and Zircaloy-4 have low, passive corrosion rates in moderate chloride concentrations (4 mM). Tests are in progress to determine the dependence and derive an analytical relationship.
- C-steel, Boral and Al-1100 have high, active corrosion rates at low pH and only slightly lower corrosion rates at pH 7 and pH 10 and form oxide or hydroxide corrosion layers that do not significantly attenuate corrosion rates (are not passivating oxides).

Key empirical observations include the following:

- Chloride concentrations of 100 mM (as NaCl) are sufficient to break down passivating oxide layers on 316L stainless steel at potentials greater than 0.5 V_{SHE} at pH 4 and at potentials greater than 0.85 V_{SHE} at pH 7 and 10.
- The measured steady state corrosion rate of 316L stainless steel ranged from 0.004 to 0.2 μm/yr.
- Carbon steel (AISI 4320) undergoes rapid, active corrosion (100 mm/yr) in pH 4 solutions regardless of NaCl concentration.
- At pH 7 and pH10 the corrosion rate of C-steel is slowed by the presence of an oxide layer (magnetite); however, this layer breaks down above 0.3 V_{SHE} at pH 7 and 0.1 V_{SHE} at pH 10 in solutions containing 100 mM NaCl.
- The measured corrosion rates for C-steel vary from 16 mm/yr to 140 mm/yr.
- Zircaloy-4 samples show relatively low corrosion rates (0.04 – 2 μm/yr) over the full pH (4 – 10) and chloride concentration range (0 – 100 mM) due to the presence of zirconium oxide on the surface. The high corrosion rate was measured at pH 10.
- The borated aluminum composite Boral was shown to undergo rapid, active corrosion with estimated corrosion rates on the same order as C-steel (≥100 mm/yr). The actively corroding phase in Boral is aluminum metal that serves as a matrix for boron carbide particles and cladding. The

B_4C particles do not appear to have corroded in any of the tests (pH 4, 7, 10), but are physically removed from the material as the surrounding Al matrix corrodes.

- Tests performed on Boral and pure aluminum (Al-1100) at pH 10 yield low corrosion rates (0.5 – 10 mm/yr) relative to results from the pH 4 and pH 7 tests at potentials below 0 V_{SHE} (based on potentiodynamic data). This is due to formation of an aluminum hydroxide layer that slows cathodic reactions at the alloy surface.

The corrosion rates measured for during the electrochemical tests were used as direct input to a new FMD/in-package chemistry model that is being developed to provide accurate long-term spent fuel degradation rates as chemical conditions (Eh, pH, speciation) evolve within a breached waste package. This new model was developed for the present study by coupling the FMD model with the reactive transport code X1t, which is a module within the Geochemist's Workbench (GWB) reaction path modeling code. The reactive transport model consists of a 1D domain discretized with 21 reaction diffusion cells and includes a single waste package cell, two cells within the bentonite backfill and then 19 other cells within the near-field host rock.

The concentration of dissolved H_2 is the key variable in the FMD model, therefore, being able to accurately model the evolution of H_2 within the waste package is essential for accurately predicting long-term spent fuel degradation rates. The reactive transport model has been used successfully to calculate the amount of H_2 produced and accumulated within a breached waste package due to the corrosion of stainless steel, carbon steel and aluminum alloys based on the experimental result described above. The GWB in-package model uses the masses, surface areas and corrosion rates of each alloy to calculate the H_2 generation rate and tracks all relevant chemical speciation reactions to provide information on in-package pH, Eh and chemistry for a 10^5 year generic repository simulation. The model includes both the diffusive and advective transport of dissolved H_2 away from the waste package to track the concentration at the fuel surface over time.

Five model scenarios for the long-term degradation rate of spent fuel within a breached waste package were evaluated using the combined GWB – FMD model. The dissolved concentrations of H_2 predicted by the GWB in-package model are directly input into the FMD model to determine the spent fuel degradation rates as a function of time. The initial sensitivity runs performed with this combined GWB - FMD model resulted in the following predictions:

- Using the alloy corrosion rates measured in the electrochemical tests presented in this study, the GWB-FMD model predicts that enough H_2 is generated to maintain concentrations higher than the threshold needed to inhibit spent fuel degradation by oxidative dissolution as long for at least 10^5 years when there is minimal advective transport of in-package solutions through the waste package (H_2 transport by diffusion only)
- In modeling cases where in-package solutions flow through the waste package (0.1 m/yr), the experimental alloy corrosion rates measured for this study produce enough H_2 to maintain concentrations higher than the threshold needed to inhibit the oxidative dissolution of spent fuel for about 500 years. After this time the spent fuel degradation rates increase rapidly by around 3 orders of magnitude due to oxidative dissolution by radiolytic H_2O_2.
- When lower alloy corrosion rates are used in the model (i.e., those used in the Yucca Mountain Project in-package chemistry model, CRWMS, 2003), the oxidative dissolution of spent fuel is inhibited for the duration of the model (10^5 years), again, as long as there is no flow through the package (H_2 transport by diffusion only).
- Including advective transport thought he waste package (0.1 m/yr) with the slower alloy corrosion rates from CRWMS, 2003 results in H_2 concentrations that inhibit the oxidative dissolution of the

fuel for 6000 years. After this time the fuel corrosion rates increase by over 2 orders of magnitude to oxidative dissolution rates caused by radiolytic H_2O_2.

The results of this study confirm the conclusions and recommendations that were identified and discussed in Jerden et al., 2017 and Jerden et al., 2018. Several of the information gaps identified in those studies remain; however, the present study has demonstrated how electrochemical testing methods can be used to address the key information gaps. Clearly, the environmental dependencies of in-package alloy corrosion rates must be taken into account in the FMD model to represent the evolving conditions in a breached waste package. Instantaneous steel corrosion rates and environmental dependencies (Eh, pH, Cl^-, T) are needed to calculate the H_2 generation rate in the FMD model. Electrochemical measurements of alloy corrosion rates provide values and dependencies on T, Eh, pH, and Cl^- conditions for active corrosion and after passivation.

6. REFERENCES

Bard, A., Faulkner, L., "Electrochemical methods: Fundamentals and Applications", John Wiley and Sons, Inc., 2001

Broczkowski, M. E.; Noël, J. J.; Shoesmith, D. W., "The inhibiting effects of hydrogen on the corrosion of uranium dioxide under nuclear waste disposal conditions" *Journal of Nuclear Materials*, vol. 346, pp. 16-23, 2005.

Buck E., Jerden, J., Ebert, W., Wittman, R., "Coupling the Mixed Potential and Radiolysis Models for Used Fuel Degradation," FCRD-UFD-2013-000290, 2013.

Buck, E., Mausolf, E., McNamara, B., Soderquist, C., Schwantes, J., "Nanostructure of Metallic Particles in Light Water Reactor Used Nuclear," *Journal of Nuclear Materials*, vol. 61, pp. 236–243, 2015.

Bethke, C.M., Yeakel, S. "The Geochemist's Workbench User's Guides, Version 10.0," Aqueous Solutions LLC, Champaign, Illinois, 2014.

CRWMS M&O 2003, "In-Package Chemistry Abstraction," ANL-EBS-MD-000037 REV 02., Las Vegas, Nevada: CRWMS M&O. ACC: MOL.20000418.0818, 2003.

Energy Solutions, "Generic Design for Small Standardized Transportation, Aging and Disposal Canister Systems," DOE Advisory and Assistance Services Contract Task Order 18, UPDATED FINAL REPORT, May 14, 2015, 317 p.

Fillmore, D.L., "Parameter Selection for Department of Energy Spent Nuclear Fuel to be Used in the Yucca Mountain License Application, Idaho National Engineering and Environmental Laboratory Report," INEEL/EXT-03-01032 Revision 1, October 2003

Grambow, B., Bruno, J., Duro, L., Merino, J., Tamayo, A., Martin, C., Pepin, G., Schumacher, S., Smidt, O., Ferry, C., Jegou, C., Quiñones, J., Iglesias, E., Rodriguez Villagra, N., Nieto, J., Martínez-Esparza, A., Loida, A., Metz, V., Kienzler, B., Bracke, G., Pellegrini, D., Mathieu, Wasselin-Trupin, G., Serres, C., Wegen, D., Jonsson, M., Johnson, L., Lemmens, K., Liu, J., Spahiu, K., Ekeroth, E., Casas, I., de Pablo, J., Watson, C., Robinson, P., Hodgkinson, D., "Model Uncertainty for the Mechanism of Dissolution of Spent Fuel in Nuclear Waste Repository," European Commission, Final Report for MICADO Project, EUR 24597, 2010.

Jerden, J., Gattu, V, Ebert, W., "Update on Validation and Incorporation of a New Steel Corrosion Module into Fuel Matrix Degradation Model", Report for Spent Fuel and Waste Science and Technology Project, Milestone #: M4SF-18AN010301017, August 6, 2018

Jerden, J., Frey, K., Ebert, W., "Spent Fuel Matrix Degradation and Canister Corrosion: Quantifying the Effect of Hydrogen", Report for Spent Fuel and Waste Science and Technology Project, Report #: SFWD-SFWST-2017-000039, February 28, 2017

Jerden J., Hammond, G., Copple J., Cruse, T., Ebert W., "Fuel Matrix Degradation Model: Integration with Performance Assessment and Canister Corrosion Model Development," FCRD-UFD-2015-000550, July 21, 2015

Jerden J. Frey K. Ebert W., "A Multiphase Interfacial Model for the Dissolution of Spent Nuclear Fuel, *Journal of Nuclear Materials*, vol. 462, pp. 135–146, 2015.

Johnson J, Anderson F, Parkhurst DL. Database thermo.com.V8.R6.230, Rev 1.11. Lawrence Livermore National Laboratory, Livermore, California; 2000

Johnson, L.H. and F. King, "Canister options for the disposal of spent fuel," Nagra Technical Report 02-11, 2003.

Kaesche, H., "Metallic Corrosion," National Association of Corrosion Engineers International, Houston, TX, 1985.

King F. and Kolar M., "Mathematical Implementation of the Mixed-Potential Model of Fuel Dissolution: Model Version MPM-V1.0," Ontario Hydro, Nuclear Waste Management Division Report No: 06819-REP-01200-10005 R00, 1999.

King F. and Kolar M., "The Mixed-Potential Model for UO_2 Dissolution MPM Versions V1.3 and V1.4," Ontario Hydro, Nuclear Waste Management Division Report No. 06819-REP-01200-10104 R00, 2003.

King, F., "Overview of a Carbon Steel Container Corrosion Model for a Deep Geological Repository in Sedimentary Rock," Nuclear Waste Management Organization Report TR-2007-01, March 2007, 71 p.

Laaksoharju M., Smellie, J., Tullborg, E-L., Gimeno, M., Hallbek, L., Molinero, J., Waber, N., "Bedrock hydrogeochemistry Forsmark site descriptive modeling SDM-Site Forsmark," SKB R-Report (R-08-47), SKB, Stockholm, Sweden, 2008.

Miller, W.M., W.R. Alexander, N.A. Chapman, I.G. McKinley, and J.A.T. Smellie, "Natural analogue studies in the geological disposal of radioactive wastes," Studies in Environmental Sciences 57, Elsevier, Amsterdam (also Nagra Technical Report NTB 93-03), 1994.

Ollila, K., "Dissolution of Unirradiated UO_2 and UO_2 Doped with ^{233}U in Low- and High-Ionic-Strength NaCl Under Anoxic and Reducing Conditions," Posiva Working Report 2008-50, 2008.

Pastina B., and LaVerne, J. A. "Effect of Molecular Hydrogen on Hydrogen Peroxide in Water Radiolysis", Journal of Physical Chemistry A 105, 9316-9322, 2001.

Posiva, "Safety case for the disposal of spent nuclear fuel at Olkiluoto – Design Basis 2012," Eurajoki, Finland: Posiva Oy. POSIVA 2012-03. ISBN 978-951-652-184-1, 2012.

Radulescu, G., "Repository Science/Criticality Analysis," Oak Ridge National Laboratory, Reactor and Nuclear Systems Division, FTOR11UF0334, ORNL/LTR-2011, Oak Ridge National Laboratory, Oak Ridge, TN., 2011.

Röllin S., Spahiu K., Eklunda U., "Determination of Dissolution Rates of Spent Fuel in Carbonate Solutions Under Different Redox Conditions with a Flow-through Experiment," *Journal of Nuclear Materials*, vol. 297, pp. 231–243, 2001.

Shoesmith, D., Kolar, M., King, F., "A Mixed-Potential Model to Predict Fuel (Uranium Dioxide) Corrosion within a Failed Nuclear Waste Container" Corrosion, vol. 59, pp. 802-816, 2003.

Shoesmith, D., "The Role of Dissolved Hydrogen on the Corrosion/Dissolution of Spent Nuclear Fuel," Nuclear Waste Management Organization, Toronto, Ontario, Canada, TR-2008-19, November 2008.

Simpson, J.P. 1989, "Experiments on canister materials for Swiss high- level waste disposal projects, Part IV. National Cooperative for the Storage of Radioactive Waste Technical Report," NAGRA-NTB-89-19, 1989.

Turnbull, A. 2009, "A Review of the Possible Effects of Hydrogen on Lifetime of Carbon Steel Nuclear Waste Canisters NAGRA," Technical Report 09-04, July 2009.

Wang Y. et al., "Used Fuel Disposal in Crystalline Rocks: Status and FY14 Progress," FCRD-UFD-2014-000060, SAND2014, Sandia National Laboratories, Albuquerque, NM., 2014.